# Hydrothermal Synthesis of Phase-Changing Vanadium Dioxide Nanoparticles and Their Use in Environmental Remediation

By

**Aaron William Daniel**

Dissertation

Submitted to the Faculty of the

Graduate School of Vanderbilt

University in partial fulfillment of

the requirements

for the degree of

DOCTOR OF PHILOSOPHY

in

Chemistry

August 10, 2018

Nashville, TN

Approved:

David E. Cliffel, Ph.D.

David W. Wright, Ph.D.

Richard F. Haglund, Ph.D.

Timothy P. Hanusa, Ph.D.

Copyright © 2018 by Aaron William Daniel

All Rights Reserved

To all those who helped along the way

ACKNOWLEDGEMENTS

*"There's a place you just can't reach unless you have a dream that's too large to bear alone."*

The road to this destination has been a long one and there are many people who deserve to be recognized. Firstly, to Dr. Cliffel: you never cease to amaze me with your wide knowledge base and ability to recall papers from twenty years ago. You've been an amazing mentor and a source of encouragement, especially when things weren't going well. To Dr. Haglund, Dr. Wright, and Dr. Hanusa; thank you for challenging me during my exams and being willing to guide me through this process.

To the members of the Cliffel lab both past and present: my nano lab compadres, Dr. Matt Casey, Dr. Dave Crisostomo, and Dr. Adam Travis. I couldn't have asked for better people to be my friends and mentors, even though we tended to distract each other more often than not. To Anna Davis—thanks for making me stop and take breathers to go raid at Broken Victory; my Pokédex thanks you, too. To the new crew—Margaret, Chris, Sara, Ethan, Dilek, & Kody—thanks for your support and encouraging words, especially in the last few months. I feel confident in the future of the Cliffel lab and I look forward to seeing what you all accomplish in the future.

To my parents, Roger and Karen. You have been unwavering pillars of support and voices of reason. I am who I am because of you both. To my sister, Ashley. Thanks for being the guinea pig and making my life that much easier. To my nephew, Logan. You were born five days before I started this journey and it has been a privilege watching you grow over the last six years and I cannot wait to see what you do with your life.

To the people who inspired me to pursue chemistry: Dr. Les Pesterfield and Arthur & Wanda Hale. Watching Dr. Pesterfield's chemistry magic show in 7$^{th}$ grade was a

turning point for me. I knew from that moment that I wanted to pursue chemistry; six years later, I was sitting in his general chemistry course. And I would not have been as nearly prepared for my undergraduate chemistry courses without the Hales. Countless students (including my parents) who passed through the halls of Ohio County High School were taught by one or both of these amazing teachers and I don't know that we will ever know the full extent of their legacy.

Finally, to the people I've never met, but have had an immeasurable impact on my life and without whom I would have undoubtedly had a mental breakdown years ago. To Jon, Claire, and Tabby from Many A True Nerd: whether you were killing everything in the Capital Wasteland, spreading the good word of Tabby throughout the galaxy, or just making a one-off video, your content has been the highlight of my day since I first encountered your channel. No matter how stressful the day had been, knowing that your newest videos were waiting for me at home made everything better. To Emile from Chuggaaconroy: your endless enthusiasm made life during grad school a little easier to bear. The thoroughness of your research and dedication to making the best videos you could was inspiring. To my Twitch friends, CptB0b and PadreReed: you two have been amazing and I am forever grateful that I decided to stop being a lurker and actually chat with you guys.

Financial support for the research presented here was provided by the National Science Foundation through the TN-SCORE program (DMR 0907619 and EPS 10040083), the Defense Threat Reduction Agency (HDTRA1-10-1-0047), and the Scialog Program of the Research Corporation for Science Advancement.

TABLE OF CONTENTS

Page

DEDICATION……iii

ACKNOWLEDGEMENTS……iv

LIST OF FIGURES…….…..…viii

LIST OF TABLES……...x

Chapter

I. INTRODUCTION……1

Background & Motivation…….….…….1
The Semiconductor-to-Metal Transition…….…….2
Applications of Vanadium Dioxide…….7
Synthesis of Vanadium Dioxide…...……...8
Control of the Transition Temperature & Hysteresis……10

II. GENERAL EXPERIMENTAL AND ANALYTICAL METHODS……..13

General Characterization…….….….13
Phase Switching Characterization…….13
Resistivity……...…..…….….…..14
Differential Scanning Calorimetry...…….…….…..….16

III. HYDROTHERMAL SYNTHESIS OF PHASE-CHANGING VANADIUM DIOXIDE NANOASTERISKS……...18

Background……18
Materials & Methods…….……...….19
Synthesis Optimizations…….……22
Fill Fraction……22
Precursor Concentration…….…24
Hydrazine……...…27
Powder XRD Analysis……...29
Particle Formation Mechanism……..31
Particle Film Characterization……33
Conclusions……37

IV. VANADIUM DIOXIDE AS AN ELECTROCATALYST FOR THE DETECTION AND REDUCTION OF 2,4,6-TRINITROTOLUENE…….39

Background……39
Methods & Materials……..40
Surface Adsorption of TNT onto $VO_2$……42
Role of Surface Oxidation……..48
Detection of Low Concentration TNT……52
$VO_2$ Electrochemistry at Elevated Temperature……53
Conclusions……55
Acknowledgements……56

V. TUNGSTEN DOPING OF VANADIUM DIOXIDE PARTICLES..……..57

Background……57
Materials & Methods……57
Characterization……58
TNT Detection & Solvent Effects……60
Conclusions……62
Acknowledgements……63

VI. CONCLUSIONS AND OUTLOOK……64

Summary……64
Future Outlook……65

Appendix

I. VANADIUM DIOXIDE AS A CATALYST FOR ELECTROCHEMICAL CARBON DIOXIDE REDUCTION……67

Background……67
Methods & Materials……..69
Results……70
Conclusions……71

II. SOLID-STATE RESISTIVITY OF ALKANETHIOLATE-PROTECTED GOLD NANOPARTICLES……72

Background……72
Materials & Methods……..73
Results……75
Conclusions……77
Acknowledgements……77

REFERENCES……78

CURRICULUM VITAE……89

LIST OF FIGURES

1.1 Crystal structure for various vanadium oxide Magnéli phases……..1

1.2 Crystal structure of conducting and semiconducting $VO_2$…….3

1.3 Wavefuctions of the HOMO and LUMO for the 3d vanadium orbitals……5

1.4 Energy diagram of monoclinic and rutile $VO_2$……..5

1.5 Pourbaix diagram for a vanadium-water system…….10

1.6 Transmittance vs. Temperature diagram……..11

1.7 DSC curves for doped $VO_2$ and relationship between dopant concentration and switching temperature……....11

2.1 Comparison of the XRD patters of $VO_2$(M) and $VO_2$(A)……13

2.2 Example of a $VO_2$ particle film……...….....…...…….…...……...15

2.3 DSC curve for synthesized $VO_2$ powder sample…….17

3.1 Schematic summary of hydrothermal $VO_2$ synthesis……..21

3.2 SEM images of $VO_2$ products at varying fill fraction……..23

3.3 SEM images of $VO_2$ products at varying precursor concentration……..25

3.4 SEM images of defects in $VO_2$ products…….27

3.5 SEM images of $VO_2$ products with excess and insufficient hydrazine……...28

3.6 SEM images of $VO_2$ product after hydrazine spike…….29

3.7 XRD comparisons at varying precursor concentrations……..30

3.8 TEM and SAED of a broken asterisk arm……...30

3.9 SEM and XRD of $VO_2$ samples prepared with varying hydrothermal reaction time..32

3.10 Transmittance vs. temperature curve for $VO_2$ particle film……..34

3.11 Four-point van der Pauw resistivity curves on $VO_2$ films…….36

4.1 Reaction mechanism for the electroreduction of TNT……40

4.2 LSVs of TNT titration on glassy carbon and $VO_2$-modified electrodes……..43

4.3 Calibration curve of TNT titration……...45

4.4 Comparison of the first and third reduction waves plotted against scan rate and square root of scan rate……..47

4.5 Calibration curve showing loss of TNT due to surface adsorption after mixing in $VO_2$ or $TiO_2$ powders……48

4.6 Raman spectrum of $VO_2$ powder at high and low laser power……50

4.7 $VO_2$ sample after taking Raman spectrum……...50

4.8 XPS spectra of TNT-detecting and non TNT-detecting $VO_2$ particles……51

4.9 Low TNT concentration calibration curve……53

4.10 Cyclic voltammograms of $VO_2$ electrodes at room temperature and 75°C……54

5.1 SEM, TEM, and EDS spectrum of $V_{0.97}W_{0.03}O_2$ particles……58

5.2 Comparison of the XRD patterns of doped and undoped $VO_2$ particles to known $VO_2$(M) and $VO_2$(R) patterns……59

5.3 Comparison of DSC curves for undoped, 1% doped, and 4% doped $VO_2$……...60

5.4 TNT titration using doped and undoped $VO_2$……..61

5.5 LSVs showing inhibition of TNT detection depending on organic wash solvent……61

A1.1 Bjerrum plot for carbonic acid……..69

A1.2 Cyclic voltammograms of C-paste and $VO_2$-modified C-paste electrodes in 0.1 M $NaHCO_3$……71

A2.1 Schematic of a proposed molecular circuit……73

A2.2 Structure of S-[4-(2-phenylethynyl)phenyl]ethynylphenyl]thiol……..75

A2.3 Comparison of $C_4$-, $C_6$-, and $C_8$-protected Au MPN film resistivities……..76

A2.4 Comparison of wired and unwired $C_6$- and $C_8$-protected Au MPN film resistivities..76

LIST OF TABLES

4.1 Breakdown of vanadium oxidation states and carbon bonding modes observed in $VO_2$ samples that do or do not detect TNT……..52

A1.1 List of electrochemical reductions for $CO_2$ and their corresponding theoretical potentials……68

CHAPTER I

# INTRODUCTION: A BRIEF HISTORY OF VANADIUM DIOXIDE

## *1.1 Background & Motivation*

Vanadium is known to form many binary and mixed-valence oxides, the most interesting of which are the Magnéli phases. These consist of vanadium oxides of the form $V_nO_{2n-1}$ with vanadium sesquioxide, $V_2O_3$, as one extreme and vanadium dioxide, $VO_2$, as the other ($n \rightarrow \infty$).[1] The crystal structure of these phases, examples of which are shown in **Figure 1.1**, can be described as rutile-type slabs composed of *n* $VO_6$ octahedra interrupted by shear planes of a corundum-like atomic arrangement.[2] All of the vanadium Magnéli phases, except for $V_7O_{13}$, exhibit sharp semiconductor-to-metal transitions (SMTs); however, they tend to occur at low temperatures (< 200 K).[2] Vanadium dioxide is unique in that its SMT, first reported by Morin in 1959, occurs relatively close to room temperature at approximately 68ºC (341 K).[3] This transition is accompanied by a change in resistivity of 3-5 orders of magnitude, a decrease in optical transmittance (especially in the infrared region), and an increase in reflectivity.[3–5] These features make vanadium dioxide an attractive candidate for use as a sensor; however, its potential chemical applications have

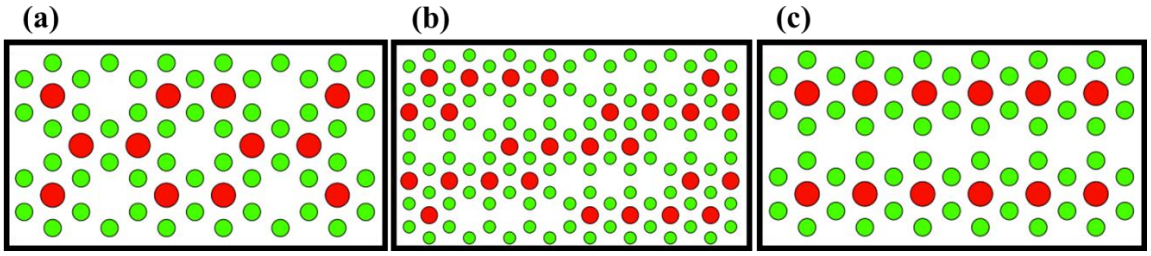


**Figure 1.1** Projections of the crystal structure for the Magnéli phases (a) $V_2O_3$, (b) $V_4O_7$, and (c) $VO_2$.[2]

remained relatively unexplored in comparison to other transition metal oxides that have been widely studied for their uses in areas such as chemical sensing,[6] catalysis,[7] solar cells,[8] data storage,[9] and energy storage.[10] Even other vanadium oxides have been studied for potential applications, such as $V_2O_5$ as a cathode material in ion intercalation batteries.[11]

Density functional theory (DFT) suggests that a catalytic event taking place at a $VO_2$ thin film could generate enough thermal energy to drive the phase transition, which could subsequently be detected either electrically (due to change in resistance) or optically (due to change in absorbance).[12] Experimentation showed that $VO_2$ thin films facilitated the catalytic electro-reduction on 2,4,6-trinitrotoluene, revealing its application as a potential electrocatalyst.[13] For many years, synthesis of $VO_2$ focused mainly on making high quality thin films that, while useful for electronic and/or optical applications, are of limited surface area and require expensive equipment to produce. Thus, the focus of this dissertation was mostly on devising a means of synthesizing large quantities of phase-changing vanadium dioxide nanoparticles, which should show enhanced sensing and catalytic activity over $VO_2$ thin films due, in part, to the significantly increased surface area.

### *1.2 The Semiconductor-to-Metal Transition (SMT)*

Above the critical phase-change temperature (68°C), the crystal structure of $VO_2$ is rutile (R, space group $P4_2/mnm$), and the material behaves as though it were a metal. In this crystal structure (**Figure 1.2a**), the lattice comprises of chains of edge-sharing $VO_6$ octahedra and the vanadium atoms form one-dimensional chains parallel to the crystallographic c-axis; each vanadium atom in any single chain is separated by a distance

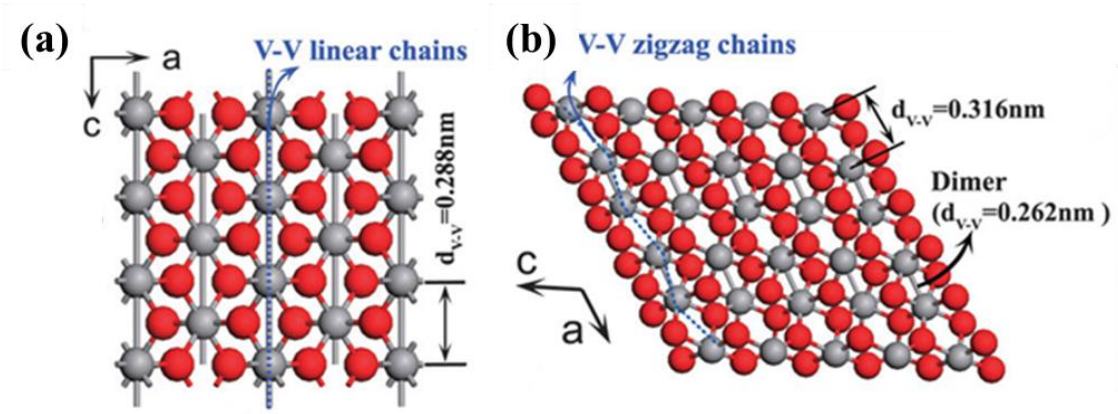


**Figure 1.2** (a) Structure of the rutile phase of $VO_2$, showing the linear chain of equidistant vanadium atoms. (b) Structure of the monoclinic phase of $VO_2$, showing the zigzag pattern and internuclear distances between vanadium atoms.[14]

of 0.288 nm. This is just below the critical separation value ($R_c$) for vanadium of 0.294 nm.[15] If the vanadium atoms are separated by a distance, $R$, longer than $R_c$, the electrons become localized on the vanadium atoms. Conversely, if $R$ is less than $R_c$, the d electrons become itinerant and are free to move between neighboring vanadium atoms. Thus, in the rutile arrangement, the interatomic distance is below $R_c$ and the 3d orbitals become delocalized over the length of each chain of octahedra, allowing for the passage of electrons, and giving rise to the metallic character of $VO_2$(R).[16]

Once cooled, however, the vanadium atoms shift out of the centers of the octahedra, forming a distorted rutile arrangement, designated $VO_2$(M) (space group $P2_1/c$; **Figure 1.2b**). This results in a zigzag pattern of vanadium atoms when viewed along the rutile c-axis (monoclinic a-axis). Accompanied by the distortion of the $VO_6$ octahedra, the vanadium atoms form dimers with two distinct V–V distances of 0.262 nm ($R<R_c$) and 0.316 nm ($R>R_c$). Goodenough theorized that the dimerized vanadium atoms share their single 3d electron in a pure covalent metal bond.[15] The HOMO and LUMO 3d wavefunctions of the electrons of the vanadium atoms, as calculated by the local density

approximation (LDA) method, can be seen in **Figure 1.3**. In the rutile phase, the wavefunction is spread out over each vanadium chain, whereas in the monoclinic phase, the wavefunction is localized on each pair of dimers.

The electronic structure of $VO_2$ in the high and low temperature phases was originally described by Goodenough.[17] As stated previously, in the high-temperature phase, the oxygen atoms are in a symmetrical octahedral arrangement around each of the vanadium atoms, which splits the V 3*d* orbitals into a lower energy $t_{2g}$ state and a higher energy $e_g$ state. The $t_{2g}$ states are further split into the $d_{||}$ and $\pi^*$ states (**Figure 1.4**), with the $d_{||}$ orbitals directed along the crystallographic rutile *c*-axis. When the vanadium atoms dimerize as a result of cooling, the $d_{||}$ state splits into lower energy bonding and higher energy antibonding states. Additionally, the $\pi^*$ band increases slightly in energy, resulting in the 0.7 eV band gap.

In the decades since its discovery, the origin and mechanism of the vanadium dioxide SMT has been a subject of much debate in the field of condensed matter physics.[18] Originally, it was believed that because of the formation of the V–V dimers, the transition occurred in accordance with Peierls' Theorem, which can be considered the solid-state analogue to the Jahn-Teller effect observed in molecules.[19] The Jahn-Teller effect describes the tendency for a molecule with a doubly degenerate HOMO occupied by two electrons to deform in such a way as to break the degeneracy; this, in turn, lowers the overall energy of the system. Similarly, Peierls' Theorem states that a one-dimensional chain of equally separated ions with one electron per ion is inherently unstable and, via phonon (lattice vibration) coupling, the ions will dimerize in order to decrease the energy of the system.

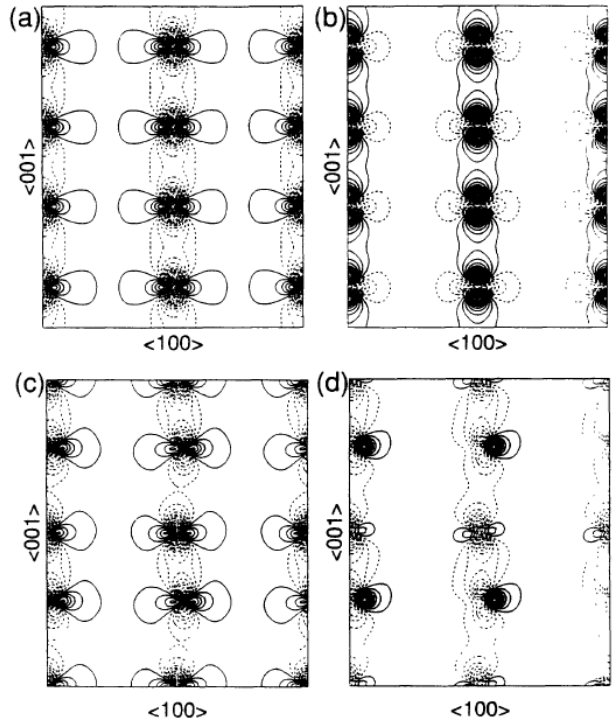


**Figure 1.3** Wavefunctions of the HOMO [(a) and (c)] and LUMO [(b) and (d)] for the 3d vanadium orbitals. In the rutile phase [(a) and (b)], the molecular orbitals stretch out over the entire chain. In the monoclinic phase [(c) and (d)], the vanadium atoms form dimers and the MO of neighboring dimers do not overlap unless excited to the LUMO.[20]

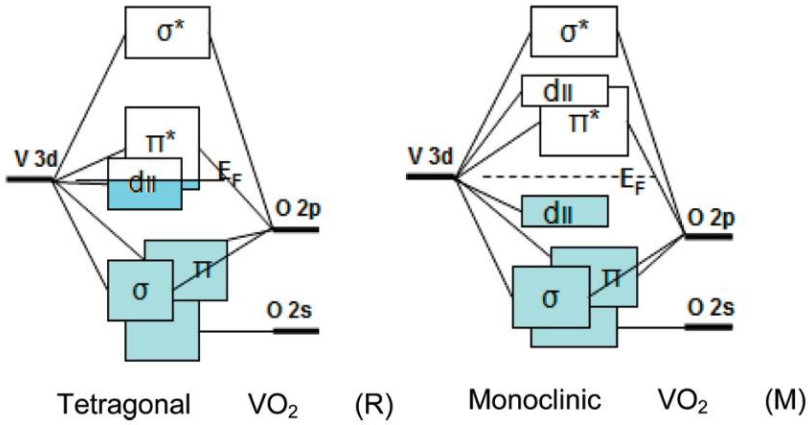


**Figure 1.4** Electronic structure of high temperature $VO_2$ (left) and low temperature $VO_2$ (right).[21]

The classic example used to explain Peierls distortion is a linear chain of H atoms ($1s^1$). Free H atoms are not as stable as the $H_2$ molecule, and it would be expected that in order to lower the energy of the system, the H atoms would dimerize to form a chain of $H_2$. The energetic cost of stretching half of the H–H bond distances is made up for by the energy gained by the shrinking of the other half. As $V^{4+}$ is a $3d^1$ ion and the V ions are equidistant in the rutile phase, the argument can be made that the phase change is likely a result of Peierls' distortion.

It has also been argued that the SMT in $VO_2$ is a result of a Mott-Hubbard transition, which finds its origin in electron correlation effects rather than changes in nuclear positioning. $VO_2$, along with other transition metal oxides, fall into a class of compounds known as strongly correlated materials.[1,22,23] As such, its electronic behaviors cannot be fully described by band theory or crystal field theory. In typical band theory, a metal is a material whose valence and conduction bands intersect and an insulator is a material whose valence and conduction bands are separated by a large energy gap; semiconductors lie between those two regimes. Mott theorized, however, that because d-bands are narrow, the coulombic interaction of d-electrons is sufficiently large that the repulsive forces result in a deviation from typical band behavior; this concept was later incorporated into the Hubbard model.[1]

Unlike other models, such as Hartree-Fock, which only deal with electron-electron interactions in a general way, the Hubbard model takes into consideration the coulombic repulsion of electrons within the same atomic orbital.[24] Only when taking this electron correlation into account do computational results begin to agree with experimental observations, such as the fact that the electronic transition can be observed on the order of

femtoseconds, which is much faster than the vanadium atoms can physically shift positions.[20,23,25] Thus, it is likely that the $VO_2$ SMT cannot be classified as either a Peierls transition or a Mott-Hubbard transition, but as a combination of both.

### *1.3 Applications of Vanadium Dioxide*

The changes in optical absorbance and reflectivity have allowed $VO_2$ to be integrated into a number of technologies including optical switches,[26] memory devices,[27] and Mott transistors.[28] One particularly interesting application is the use of $VO_2$ in "smart windows," which take advantage of the thermochromic properties of various materials by coating or impregnating windows with them.[29] It is estimated that as much as 30–40% of the world's primary energy is used every year in lighting and climate control of buildings and vehicles.[30] Controlling the amount of solar infrared radiation that is allowed into buildings would greatly improve their energy efficiency and aid in reducing carbon emissions. There are, of course, many challenges that must be overcome before smart windows can be used commercially, such as the relatively high switching temperature (which can be overcome by doping[31]) and opacity in the visible region.

It has also been shown that the SMT of $VO_2$ could be exploited in a variety of thermochromic or thermoelectric sensors. Warnick *et al.* described the theory behind using a $VO_2$(M) thin film substrate modified with Fe-porphyrin to detect an analyte molecule such as 2,4-dinitrotoluene (DNT).[12] According to their computational model and reaction mechanism, the thermal energy released from desorption of a catalytically oxidized DNT molecule from an Fe-porphyrin would be enough to drive the SMT so that it could be detected either optically or electrically, provided that the film was held at a temperature

just below the transition begins. Previous work in the Cliffel group has shown that $VO_2$(M) thin films can be used directly as an electrode for the electrochemical reduction of the nitro groups of 2,4,6-trinitrotoluene (TNT) to amines.[13] Utilizing adsorptive stripping voltammetry, TNT was detected at concentrations as low as 1 ppb, which is comparable to the most sensitive modified electrodes used in electrochemical TNT detection. Using electrodes modified with hydrothermally synthesized $VO_2$ particles to detect TNT is the focus of Chapter IV.

### *1.4 Synthesis of Vanadium Dioxide*

The monoclinic $VO_2$(M) and rutile $VO_2$(R) are not the only possible crystal structures of $VO_2$; however, the SMT only occurs between those two phases. To date, there are at least ten known and characterized phases of $VO_2$ and $VO_2$ hydrates. The most common phases include the tetragonal $VO_2$(A),[32] monoclinic $VO_2$(B),[33] monoclinic $VO_2(M_1)$,[34] monoclinic $VO_2(M_2)$,[35] and tetragonal $VO_2$(R).[36] Less common phases include the tetragonal $VO_2 \bullet ½H_2O$, also known as $VO_2$(C),[37] and monoclinic $VO_2$(D).[38]

To this point, the low temperature phase of $VO_2$ has been represented as (M). However, there are actually two monoclinic phases given the designation M and are differentiated as $M_1$ and $M_2$. The monoclinic phase that has been the focus thus far is more correctly designated as $M_1$. The $M_2$ phase is very similar to $M_1$, however, only one-half of the vanadium atoms are dimerized (in alternating pairs). It is theorized that the $M_2$ phase is a metastable transition state between $M_1$ and R, though it is typically only seen when stress is applied either directly to the crystal or by the substrate (in the case of epitaxial

strain in a thin film).[22] Any reference to $VO_2$(M) in this dissertation refers specifically to the $M_1$ phase.

The synthesis of $VO_2$(M) often involves the initial synthesis of one of the other $VO_2$ polymorphs. At elevated temperatures, $VO_2$(R) is the most thermodynamically stable polymorph, and thus, with sufficient heat and time, all of the $VO_2$ polymorphs will convert to $VO_2$(R).[16,39,40] Upon cooling, $VO_2$(R) will reversibly convert to $VO_2$(M) in accordance with the SMT. The most common methods for the synthesis of $VO_2$ include magnetron sputtering, pulsed laser deposition (PLD), chemical vapor deposition (CVD), sol-gel chemistry, and hydrothermal synthesis.[4,16,41–43] Sputtering, PLD, CVD, and sol-gel are energy intensive, inefficient, or require the use of expensive equipment and/or chemical precursors.

While these methods are capable of producing high-quality thin films for electro-optic and electronic applications, they are generally incapable of producing large quantities of material for applications such as catalysis. Hydrothermal synthesis, however, offers a way to produce large quantities of product from inexpensive precursors such as $V_2O_5$ and is readily scalable. Vanadium dioxide hydrothermal syntheses have been studied extensively over the last twenty years; however, a direct route to $VO_2$(M) has remained elusive until recently. This can be attributed to the rich vanadium chemistry observed in aqueous solutions, which can be visualized in a Pourbaix diagram (**Figure 1.5**). Chapter III focuses on recent efforts to refine the process of making phase-changing $VO_2$ hydrothermally without the need for an annealing step.

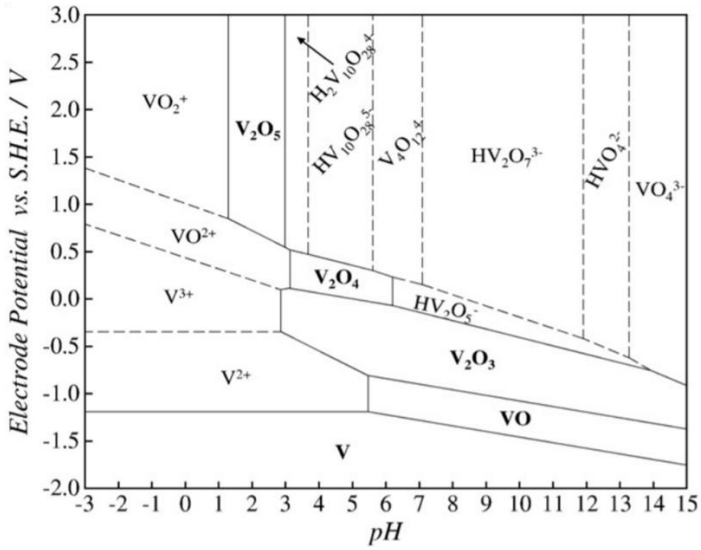


**Figure 1.5** Pourbaix diagram for a vanadium-water system at 25°C and a vanadium activity of $10^{-2}$.[44]

### *1.5 Control of the Transition Temperature and Hysteresis*

As has been established, the transition temperature of $VO_2$ is 68°C, however this is only in reference to bulk crystals and considers only the transition from $M_1$ to R. The transition temperature can be affected by many factors, some of the most important of which are crystal size and doping. The size of the grains in a $VO_2$ thin film (or the size of $VO_2$ nanoparticles) show a direct relationship with transition temperature: that is to say, as the grains or particles get smaller, the transition temperature decreases.

If the resistivity, reflectivity, or absorbance of $VO_2$ is plotted as a function of temperature, a hysteresis effect is observed whereby the transition from R to M takes place at a lower temperature (**Figure 1.6**). In bulk crystals, this hysteresis may be as narrow as 1°C. For thin films, this hysteresis may be as wide as 10-15°C and, for nanostructured $VO_2$, hysteresis widths as wide as 30-35°C can be observed. Suh *et al.* showed that the width and shape of the hysteresis can be attributed to a competition between crystallinity and grain size.[45]

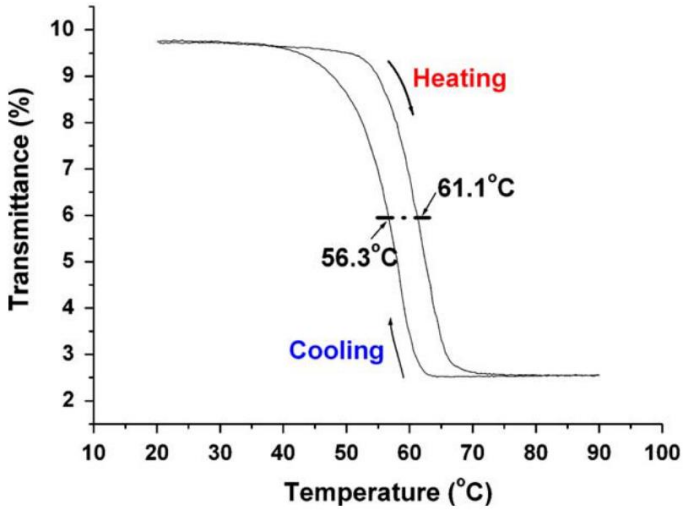


**Figure 1.6** An example transmittance vs. temperature plot of $VO_2$ crystals during a heating-cooling cycle, revealing a hysteresis loop.[46]

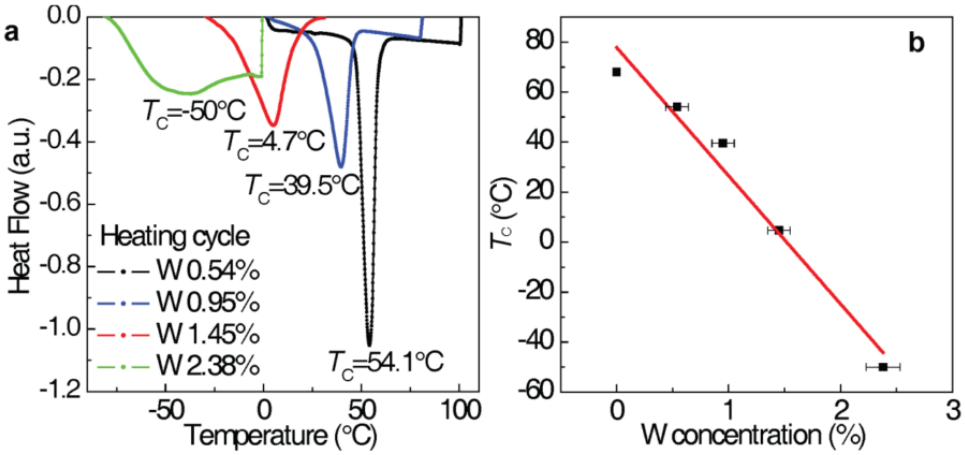


**Figure 1.7** (a) Differential scanning calorimetry (DSC) measurements of $W_xV_{1-x}O_2$ single crystals at varied W-dopant concentrations. (b) Switching temperature as a function of W-doping concentrations.[47]

Doping has also been shown to raise or lower the transition temperature of $VO_2$(M) depending on the identity and amount of dopant used.[30] High valent metals such as $W^{6+}$, $Mo^{6+}$, $Ta^{5+}$, $Nb^{5+}$, and $Ru^{4+}$ have been reported to lower the transition temperature, whereas low valent metals and metalloids such as $Ge^{4+}$, $Al^{3+}$, and $Ga^{3+}$ will increase the transition temperature.[17] X-ray absorption fine structure (XAFS) spectroscopy, a technique capable of providing information about the local structure around an atom, reveals that the immediate vicinity around a $W^{6+}$ within the $VO_2$ lattice has rutile symmetry, resulting in "metallic nanopuddles." These nanopuddles act as nuclei that lower the energy required to start the transition to $VO_2$(R).[18] Hexavalent tungsten has been heavily studied as a $VO_2$ dopant, as it capable of reducing the transition temperature by 20–25ºC per atomic percent (**Figure 1.7**).[47] However, the addition of a dopant also causes the transition to become less sharp and the change in optical transmittance greatly decreases.[30] We explore how doping affects the $VO_2$ nanoparticles' phase behavior and ability to detect TNT in Chapter V.

CHAPTER II

# GENERAL EXPERIMENTAL AND ANALYTICAL METHODS

## *2.1 General Characterization*

Characterization of $VO_2$ materials is mostly independent of the synthetic method used. Powder X-ray diffraction is used to distinguish the $VO_2$ polymorphs depending on how x-rays constructively or destructively interfere with one another within the crystal lattice (**Figure 2.1**). Scanning electron microscopy (SEM) and atomic force microscopy (AFM) reveal the nanostructured morphology of particles and/or films. Transmission electron microscopy (TEM), coupled with single area electron diffraction (SAED), reveals details about crystallinity and crystallographic orientation of $VO_2$ nanoparticles.

## *2.2 Phase Switching Characterization*

The phase transition of $VO_2$ can be monitored by several different methods, which include UV-Vis-IR spectroscopy, Raman spectroscopy, zeta potential, and resistivity.

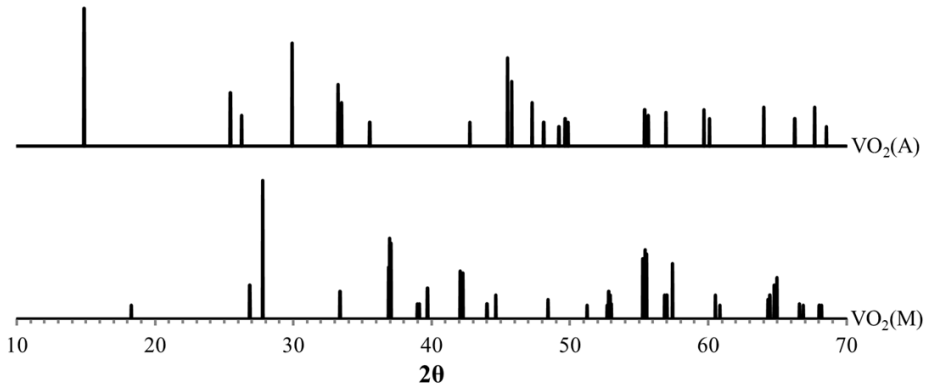


**Figure 2.1** Comparison of the XRD patterns between monoclinic $VO_2$(M) and tetragonal $VO_2$(A), two common polymorphs encountered when hydrothermally synthesizing $VO_2$.

### *2.2.1 Resistivity*

One of the most common methods of studying the phase transition in bulk crystals and thin films is by measuring the electrical resistance as a function of temperature. Typically, resistance is measured via a two-probe system whereby the current and potential are measured simultaneously. While this will provide accurate temperature data, the true value of the resistivity will be inaccurate in part due to a phenomenon known as contact resistance. In a two-probe setup, the current that passes through the contacts induces a potential drop between them, which is measured by the device as resistance; however, this resistance acts as though it were in series with the resistance of the sample and thus cannot be decoupled from it.

Contact resistance can be eliminated from the measurement by the use of a four-point probe system. As the name suggests, four different probes are in contact with the sample. One pair of probes applies a current to the sample while a second set of probes in parallel with the other is used to measure the potential drop across the sample. In this way, the potential drop between the current-applying probes is rendered irrelevant and contact resistance is excluded from the measurement.

An important variation of four-probe resistivity measurements is known as the van der Pauw method.[48,49] In van der Pauw's method, several criteria need to be met to assure accuracy of the results, which include (1) the sample should be flat, uniformly thick, and much thinner than the length of the sample; (2) the sample should be contiguous with no isolated holes; (3) the sample should be homogenous; (4) the probe contacts should be placed at the edges of the sample; (5) the area of the contacts should be, at minimum, one order of magnitude smaller than the total area of the sample.

A simple schematic of a four-point probe setup in which the probes are in a square arrangement (including the probe numbering) is shown in **Figure 2.2**. The average resistivity, $\rho$, of a sample is given by the formula

$$\rho = R_s t \tag{2.1}$$

where $R_s$ is the sheet resistance and $t$ is the thickness of the sample. Following the numbering scheme in **Figure 2.2**, the resistance measured when a current is passed from probe 1 to probe 2 and the potential drop between probe 3 and probe 4 is given by Ohm's Law

$$R_{12,34} = \frac{V_{34}}{I_{12}} \tag{2.2}$$

This provides the "vertical" resistance of the film. Another measurement is made in the "horizontal" direction by passing a current from probe 2 to probe 3 and measuring the potential drop between probe 4 and probe 1. The relationship between the measured resistances and the overall sheet resistance, $R_s$, is given by the van der Pauw formula

$$e^{-\pi R_{12,34}/R_s} + e^{-\pi R_{23,41}/R_s} = 1 \tag{2.3}$$

Other factors may be considered to improve the accuracy and precision of the measurements. The Lorentz reciprocity theorem states that the measured resistance of a

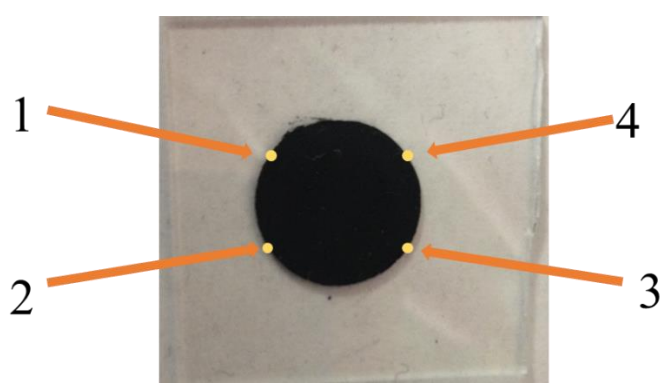


**Figure 2.2** A film sample showing the location and ordering pattern of the probe contacts.

material should remain unchanged when the source and detector are interchanged.[50] Thus, $R_{12,34}$ and its reciprocal ($R_{34,12}$) can be averaged and $R_{23,41}$ and its reciprocal ($R_{41,23}$) can be averaged as $R_{vertical}$ and $R_{horizontal}$, respectively, and replaced into **Equation 2.3** as

$$e^{-\pi R_{vertical}/R_s} + e^{-\pi R_{horizontal}/R_s} = 1 \qquad \textbf{(2.4)}$$

Additionally, the polarity of the measurements can be reversed to increase the accuracy, whereby the direction of the current can be reversed ($R_{21}$ rather than $R_{12}$). This can cancel out any variations in the voltage that may result from phenomena such as the Seebeck effect[51] (conversion of heat directly into electricity at the junction of two metals or semiconductors). In this way, $R_{vertical}$ and $R_{horizontal}$ are made up of the average of four independent measurements each

$$R_{vertical} = \frac{R_{12,34}+R_{21,43}R_{34,12}+R_{43,21}}{4} \qquad \textbf{(2.5)}$$

This method of taking reciprocal and reverse polarity measurements is used in all resistivity measurements presented in Chapter III and Appendix II.

### *2.2.2 Differential Scanning Calorimetry*

Developed in 1962, differential scanning calorimetry (DSC) is a thermo-analytical technique that measures the difference in the amount of heat required to raise the temperature of a sample and a reference as a function of temperature.[52] The basis for the technique is that, when a material undergoes some kind of physical transformation (like a phase transition), the heat required to keep the sample at the same temperature as the reference will either increase or decrease. These transformations may include transitions between phases of matter (e.g., melting), crystal structure phase transitions (such as in

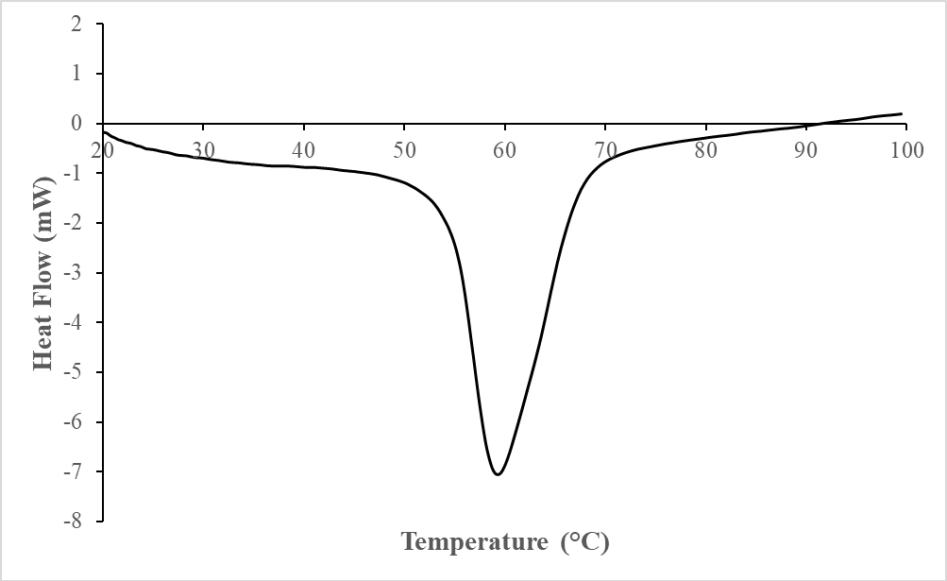


**Figure 2.3** DSC curve of a sample of vanadium dioxide. Scan rate: 20°C/min.

$VO_2$), or protein denaturing. It is also widely used in the field of polymer characterization to measure glass transitions, degradation, and purity.[53]

The output of a DSC experiment, shown in **Figure 2.3**, is a graph of heat flow vs. temperature. In this particular example, a sample of $VO_2$ powder was tested against an aluminum reference. Because the phase change from $VO_2$(M) to $VO_2$(R) is endothermic, the peak is in the negative direction. Conversely, if the change from (R) to (M) were recorded, it would appear as a positive peak (though shifted down in temperature due to the hysteresis).

CHAPTER III

# HYDROTHERMAL SYNTHESIS OF PHASE-CHANGING VANADIUM DIOXIDE NANOASTERISKS

## *3.1 Background*

Vanadium dioxide ($VO_2$) is a unique transition metal oxide that undergoes a first-order phase transition at approximately 340 K from a semiconducting monoclinic phase (M, space group $P2_1/c$) to a conducting rutile phase (R, space group $P4_2/mnm$). During this semiconductor-to-metal transition (SMT) the resistivity decreases up to five orders of magnitude in bulk crystals and three to five orders of magnitude in thin films. Additionally, there is an increase in the optical absorbance and reflectivity of the material, especially in the infrared,[3–5] which has led to the incorporation of phase-changing $VO_2$ into various types of metamaterials.[54–57] Metamaterials are artificial materials composed of nanoscale subunits that interact in novel ways with electromagnetic radiation.[58,59] Typically, $VO_2$ is used as a substrate upon which nanoarrays of Au or Ag are deposited.[60–62]

The most common methods for the synthesis of $VO_2$(M) are magnetron sputtering, pulsed laser deposition (PLD), chemical vapor deposition (CVD), sol-gel chemistry, and hydrothermal synthesis.[4,16,41–43] Sputtering, PLD, CVD, and sol-gel, are energy intensive, inefficient, or require the use of expensive equipment and/or chemical precursors. While these methods are capable of producing high quality thin films for electro-optic and electronic applications, they are generally incapable of producing large quantities of material for other applications such as catalysis. However, hydrothermal synthesis offers a way to produce large quantities of product from inexpensive precursors such as $V_2O_5$.

Although $VO_2$ hydrothermal syntheses have been well studied over the last twenty years, a direct route to $VO_2$(M) has remained elusive. For most hydrothermal methods, the precursors are combined and subjected to hydrothermal conditions at temperatures ranging from 150–250ºC for one hour to several days.[42,63–66] These precursor and reaction conditions result in the formation of one of the several $VO_2$ polymorphs. The product is typically then collected and subjected to an annealing step, which forces the conversion of the product to the R phase. When cooled, the product relaxes to the M phase in accordance with the SMT. Recently, Son *et al.* devised a method capable of producing crystalline $VO_2$(R) directly *in situ* during hydrothermal treatment without the need for annealing.[41] The morphology of their particles resembles a six-armed "asterisk" structure. In our work, we optimized their synthetic parameters and have produced a variety of asterisk morphologies in relatively large quantities. We also report the first description of the collective phase transition and resistivity characteristics of a drop-cast film of $VO_2$(M) particles on thin glass substrates via four-point van der Pauw resistivity measurements.

### *3.2 Materials & Methods*

$V_2O_5$ (solid, 99.6%) and $N_2H_4{\cdot}H_2O$ (liquid, 98%) were purchased from Sigma-Aldrich. $H_2SO_4$ (liquid, 98%) and NaOH (solid, 99%) were purchased from EMD Chemicals. All materials were used without further purification. The water used in all experiments was deionized to a resistivity of 18.2 MΩ/cm.

$VO_2$(M) particles were synthesized as outlined by Son *et al.*[41] with modifications; a general reaction scheme is shown in **Figure 3.1**. Briefly, $V_2O_5$ (0.45 g, 2.5 mmol) was slurried with 10 mL of water in a 250 mL three-neck flask, stirred vigorously for 15

minutes, and held in a water bath at 90ºC. The slurry was then acidified with $H_2SO_4$ (750 μL) and stirred for an additional five minutes. Hydrazine monohydrate (250 μL) was then added rapidly. In later experiments, scalar multiple amounts of the preceding chemicals were used. The pH of the solution was then adjusted to 4.0 using 1 M NaOH, resulting in the formation of a purple precipitate. The precipitate was collected via vacuum filtration and washed several times with water. Without drying, the precipitate was transferred to a Teflon cup (43 mL capacity) with 25 mL of water and stirred vigorously for one hour before being transferred to a stainless-steel autoclave. Hydrothermal treatment was carried out at 230ºC for 48 hours in a muffle furnace, after which the autoclave was allowed to cool down to room temperature naturally. The resulting blue/black product was collected via centrifugation, washed several times with water and ethanol, and dried in air at 100ºC for 18 hours. The particles from various synthetic modifications were denoted as $VO_2$-*x*mmol V (e.g., $VO_2$-5mmol refers to a sample in which 2.5 mmol of $V_2O_5$ was used to synthesize the vanadium precursor).

Films of $VO_2$ particles were drop cast onto thin glass substrates covered with an electroplating mask that exposed a 1.00 $cm^2$ circular area. A suspension of particles was prepared by mixing 1.5 mg of particles with 250 μL of water and sonicating for one minute to ensure homogeneity. After drop casting, the films were dried under reduced pressure for at least one hour.

Particles were characterized using scanning electron microscopy (SEM) images obtained using a Hitachi S4200 microscope operating at 10kV accelerating voltage. Transmission electron microscopy (TEM) images and selected area electron diffraction (SAED) images were obtained using a FEI Tecnai Osiris operating at 200 kV. Powder

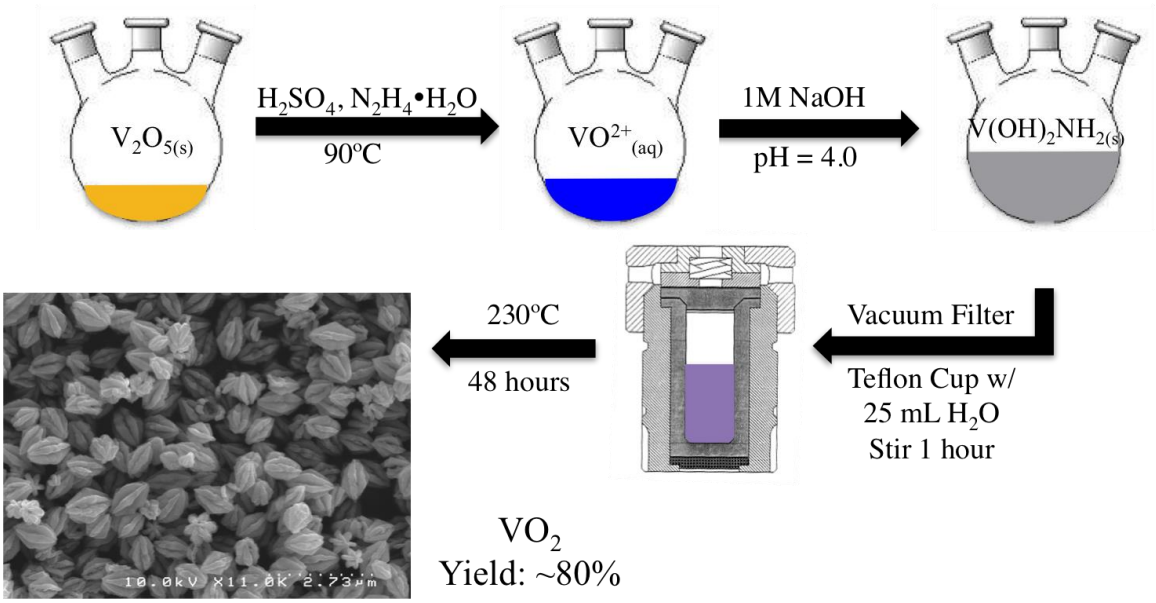


**Figure 3.1** Schematic summary of the synthesis of vanadium dioxide.

XRD (pXRD) patterns were obtained using a Scintag X1 Powder X-Ray Diffractometer with Cu Kα radiation (λ = 1.5418 Å). $N_2$ adsorption-desorption surface area analysis was measured using a Micromeritics ASAP 2020 at -196ºC (77 K) with nitrogen as the analysis gas. Stylus profilometry was performed using a Veeco Dektak 150 Profilometer in tapping mode. van der Pauw four-point resistivity measurements were made on an MMR Variable Temperature Hall Effect Measurement System using constant applied current ($i$ = 100 nA) with measurements taken every 2 K.

### *3.3 Synthesis Optimizations*

Son *et al.* reported three main products of their hydrothermal synthesis: $VO_2$(B) nanorods, $VO_2$(M) microrods, and $VO_2$(M) asterisks. They describe the reaction conditions required to synthesize each type of product, only one of which did they report was capable of producing 100% $VO_2$(M) (as determined by XRD), which is the procedure detailed above. To ensure the formation of $VO_2$(M), reaction conditions were optimized to synthesize only asterisk-shaped particles.

#### *3.3.1 Fill Fraction*

The fill fraction of a hydrothermal synthesis refers to how much solvent is used during hydrothermal treatment versus how much volume is available in the reaction vessel; this has a strong influence on the internal pressure of the reaction vessel. In Son *et al.*'s procedure, they used a fill fraction of 0.43 (10 mL water in 23 mL vessel). To test the effect of fill fraction, hydrothermal treatment of the vanadium precursor was performed using 10.0 mL, 20.0 mL, 25.0 mL, and 30.0 mL, corresponding to fill fractions of 0.233, 0.465,

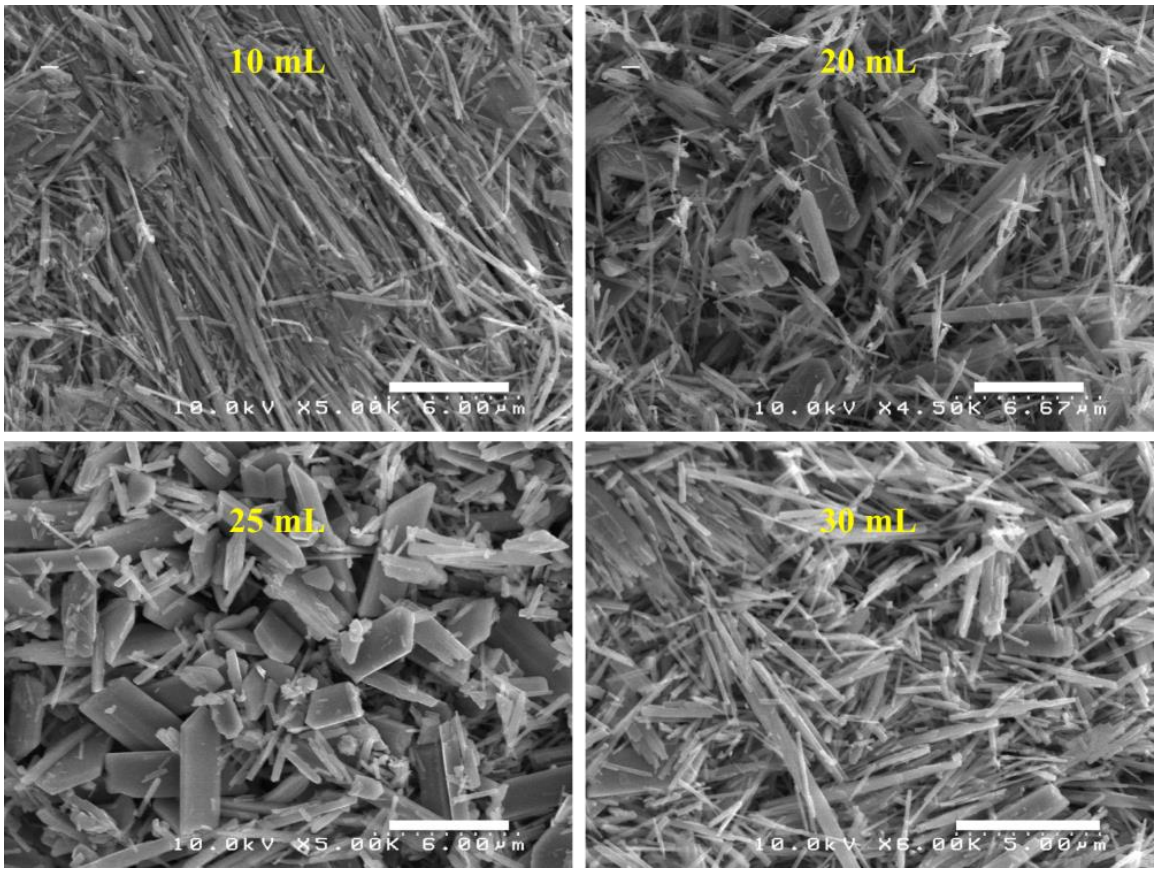


**Figure 3.2** SEM images of $VO_2$ samples synthesized using fill fractions of 0.233 (10.0 mL), 0.465 (20.0 mL), 0.581 (25.0 mL), and 0.698 (30.0 mL). The 0.233 sample failed to produce $VO_2$. Because it synthesized mostly plates, 25 mL was taken to be optimal for synthesis of asterisks. Scale bars represent 5.0 µm.

0.581, and 0.698, respectively, with a 43 mL reaction vessel. The hypothesis was that larger fill fractions would result in higher quality product and that higher pressures would result in the preferential formation of asterisks. One theory for their formation, proposed by Ji *et al.*,[46] is that three plates fuse together into the six-armed asterisk structure.

Representative SEM images of synthesized particles from each fill fraction are shown in **Figure 3.2**. When 10.0 mL of water was used, $VO_2$ did not form, but rather, the product was a green powder that, according to energy-dispersive X-ray spectroscopy (EDX), was a different oxide of vanadium; pXRD analysis confirmed it to be the mixed valent oxide $V_3O_7 \cdot H_2O$ (JCPDS No. 28-1433). This green compound remained as a secondary product in the rest of the fill fraction experiments. At 20.0 mL and 30.0mL, there was noticeable formation of plates, which was a positive sign of the presence of $VO_2$(M), but needles and nanorods were still the major product. However, when 25.0 mL was used, plates were formed almost exclusively and, as such, 25.0 mL of water was used for all future hydrothermal reactions.

### *3.3.2 Precursor Concentration*

Standard nucleation theory and the LaMer model for burst nucleation state that increasing the precursor concentration results in the formation of smaller particles.[67] With the goal of making an electrode material and catalyst, it is desirable to make smaller particles in order to increase the surface area available for reactions. To study the effect of increased precursor concentration during hydrothermal treatment, the amount of precipitate reacted was increased by integer multiples; representative SEM images are shown in **Figure 3.3**. After cooling, the $VO_2$-5mmol product formed a pellet at the bottom of the

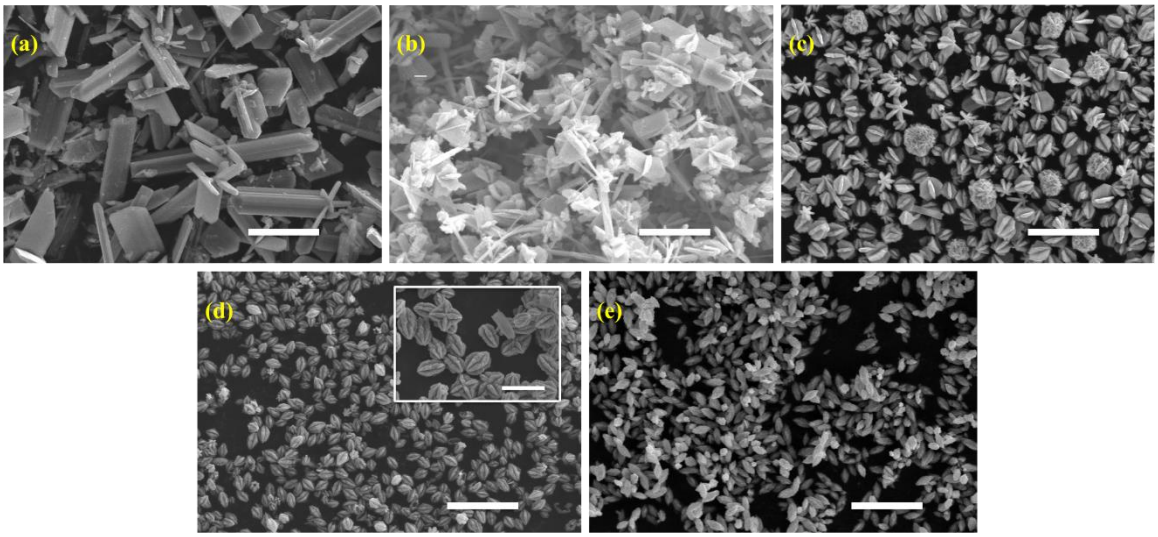


**Figure 3.3** Representative SEM images of (a) $VO_2$-5mmol, (b) -10mmol, (c) -15mmol, (d) -20mmol, and (e) -25mmol. Inset of (d) shows asterisk tetramers. Scale bars: 5.0 μm.

Teflon cup consisting of a green outer layer (the $V_3O_7 \cdot H_2O$ mentioned in the previous section) and a dark blue interior. The dark blue product consisted of polydisperse rectangular plates, ranging in length from 1–10 μm, though some particles with an asterisk morphology were also observed.

$VO_2$-10mmol particles exhibited a snowflake-like asterisk morphology. Similar to $VO_2$-5mmol particles, the asterisks were polydisperse, ranging in size from 1–5 μm, and tended to be highly asymmetric with regards to arm length. Previously, researchers have theorized that the asterisk morphologies occurred when a $VO_2$(A) rod or plate splintered due to strain during conversion to $VO_2$(R) and formed a $VO_2$(R) embryo, which then grew into an asterisk.[46,68] The $VO_2$-10mmol particles seem to support this formation mechanism, as it is possible to observe the "parent" plate from which the additional four arms grow.

$VO_2$-15mmol particles were significantly smaller (1.2 ± 0.2 μm in length, 1.0 ± 0.2 μm in width) than the $VO_2$-10mmol particles and the arms became truncated. This likely resulted from the formation of more nuclei during the initial stages of particle formation, and subsequently less available material for arm growth.[69] Interestingly, the formation of anomalous fused asterisk clusters was also observed. These clusters were approximately 1–3 μm in diameter and were composed of very small asterisks (0.5 ± 0.2 μm in length and width). These fused asterisk clusters appeared in multiple synthesis trials, but only when 15 mmol of precursor was used.

In $VO_2$-20mmol samples, the asterisks clusters were not observed and again, the asterisks became smaller (1.1 ± 0.2 μm in length, 0.7 ± 0.2 μm in width) and further truncated. Additionally, visible defects were seen in the asterisks, such as missing or chipped arms, as shown in **Figure 3.4**. This was possibly due to strain caused during

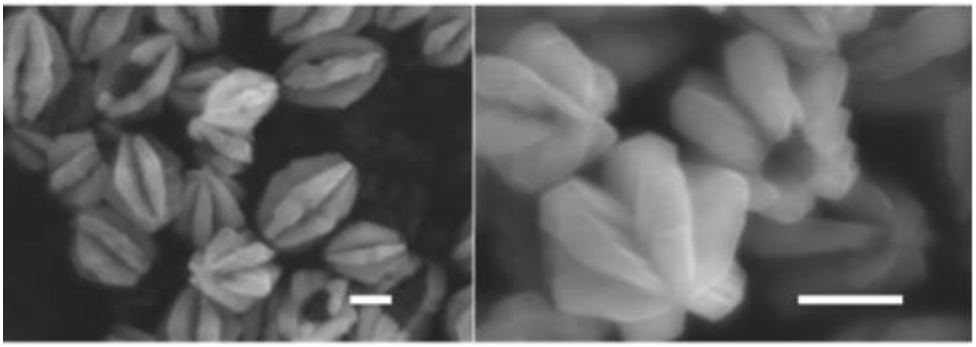

**Figure 3.4** Defects in the product of the $VO_2$-20mmol synthesis, including missing/broken arms (left) and hollow interiors (right). Scale bars: 500 nm

conversions from the R phase to the less dense M phase. Additionally, **Figure 3.4** revealed particles in which a vacancy was observed in the core. Based on this observation, it is likely that these truncated asterisks, while similar in morphology to the long-armed asterisks, were formed by a different mechanism than the one described by Ji *et al.*,[46,68] which would not account for this phenomenon. The mechanism by which these particles formed will be discussed below. $VO_2$-25mmol particles were also synthesized, however, their morphology did not evolve beyond sharp ellipsoids. The particles were 1.3 ± 0.3 μm in length and 0.5 ± 0.2 μm in width.

### *3.3.3 Hydrazine*

It was theorized by Son *et al.* that the hydrazine plays a critical role in the formation of the asterisks, as attempting the synthesis without it does not produce any. This is not to say that only reactions using hydrazine as the reducing/coordinating agent are capable of producing asterisks. Others have shown that hydrothermal reactions utilizing bidentate ligands, such as oxalate ion, as the reducing/coordination agent to make $VO_2$ produce similar snowflake asterisk structures.[46,70] As it does play some role, the volume of hydrazine used during the synthesis of the precursor was varied; these effects

were studied only on the 20 mmol scale. Initially, the amount of hydrazine was increased by 33% (from 1.00 mL to 1.33 mL), which was hypothesized to decrease the size of the particles, as there would be more ligand available to bind to the surfaces. However, a large increase in size of the particles was observed (averaging more than 3 μm in length), as well as an increase in polydispersity (**Figure 3.5**).

The effect of starving the system of hydrazine was also studied. During the reduction of $V_2O_5$ to $VO^{2+}$, the hydrazine is introduced rapidly. To starve the system of hydrazine, the hydrazine was added in dropwise until the solution just turned a clear blue, signaling the complete reduction of all of the $V_2O_5$. The reaction was then carried out with no further changes. The resulting product was oddly textured, almost clay-like, as opposed to the particulate product of other reactions. SEM analysis revealed that there were no asterisks in the starved product, which further supports Son *et al.*'s hypothesis of hydrazine's critical role (**Figure 3.5**).

An additional experiment (using 5 mmol precursor) was performed whereby the amount of hydrazine used in the synthesis of the $V(OH)_2NH_2$ precursor remained

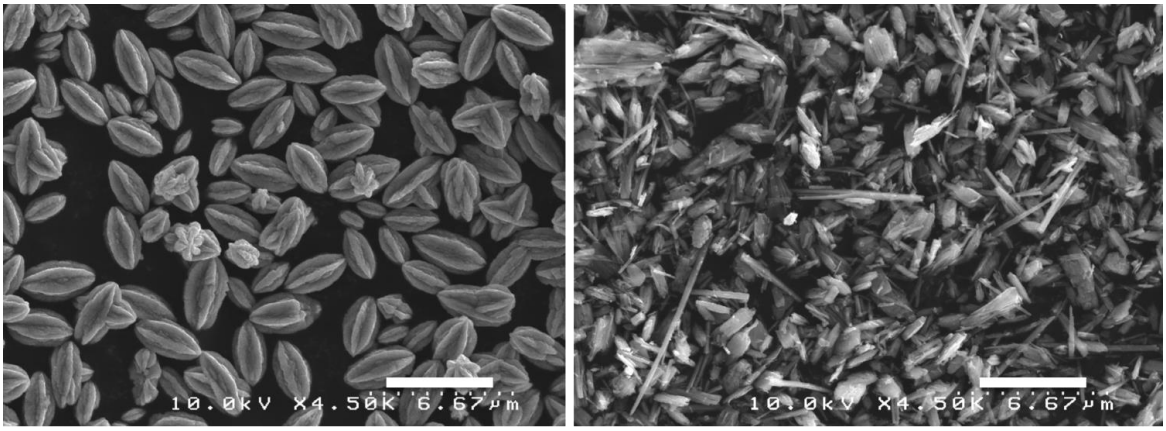


**Figure 3.5** Effect of increased hydrazine in the preparation of the $V(OH)_2NH_2$ precursor on the $VO_2$ particles (left) and effect of decreased hydrazine (right). Increasing hydrazine results in larger particles, whereas decreasing hydrazine results in no asterisks. Scale bars represent 5 μm.

unchanged, but a small additional amount of additional hydrazine (10% of the volume used during the initial reduction) was injected five minutes prior to the transfer of the cup to the autoclave while the precursor/water mixture was still stirring. Increasing the hydrazine was hypothesized to improve the quality of the nanoparticles and/or decrease their size. This change resulted in the formation of large aggregates of $VO_2$ nanocrystals, roughly 50–100 nm in size (**Figure 3.6**). TEM was used to attempt to get more highly resolved images but was not able to provide any significant improvement. In making the TEM samples, however, it was discovered that these particles were not water stable and oxidized to $V^{5+}$ in less than 24 hours (determined by the solution turning pale yellow, indicative of aqueous $V^{5+}$). This instability would make the particles unsuitable as an electrode material for aqueous systems (such as TNT detection).

### *3.3.4 Powder XRD Analysis*

Powder XRD analysis of the $VO_2$ preparations is shown in **Figure 3.7**. As synthesized, the products appeared to be predominately monoclinic $VO_2$, though a minor contribution from the metastable, tetragonal $VO_2$(A) phase was also observed. Increasing

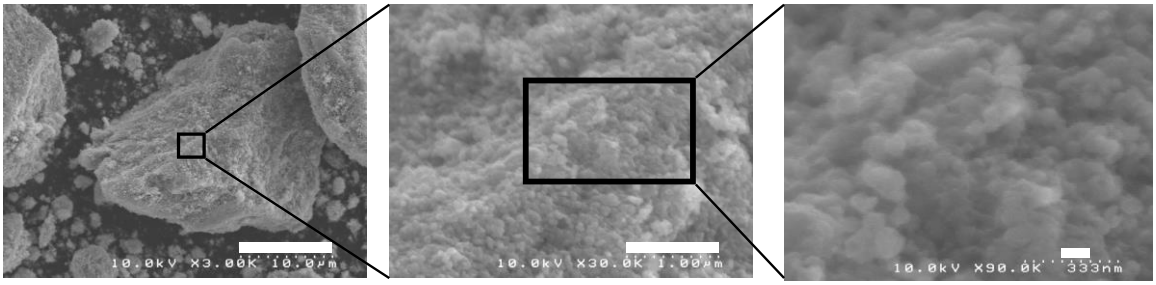


**Figure 3.6** Effect of "spiking" the hydrothermal reaction with a small portion of hydrazine. The small, 30-50 nm crystals aggregate into large particles. Boxes indicate where the images were zoomed. Scale bars represent, from left to right, 10 µm, 1 µm, and 100 nm.

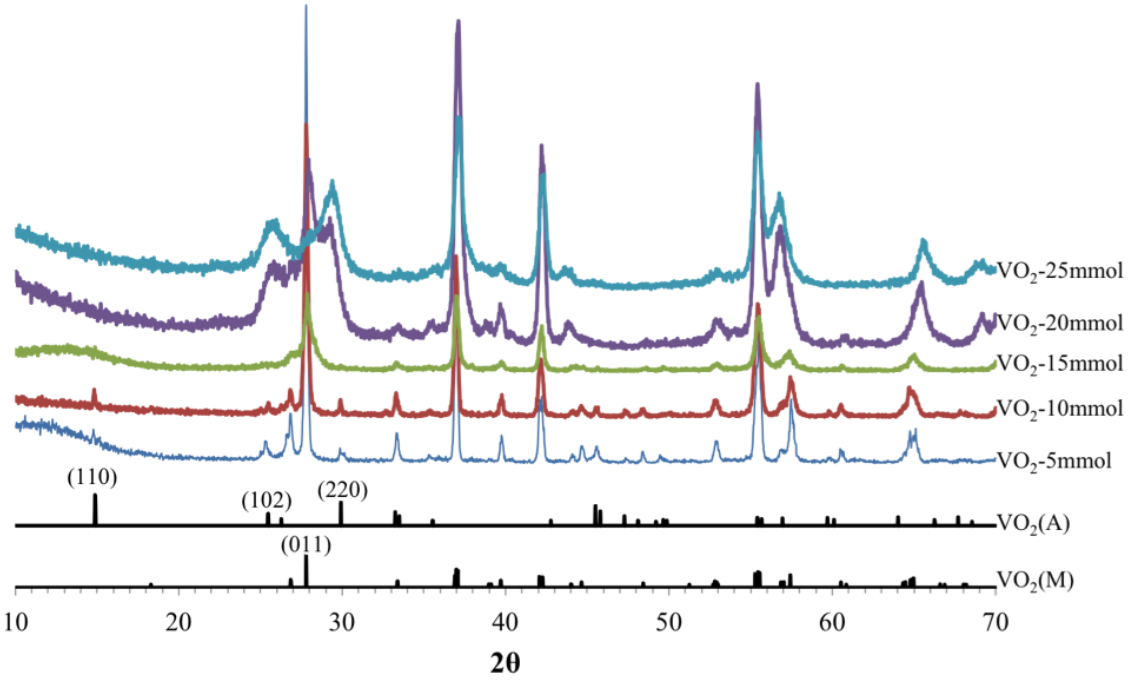


**Figure 3.7** Diffraction patterns obtained from the various synthesized $VO_2$ powders matched to $VO_2$(M) (JCPDS No. 43-1051) and $VO_2$(A) (JCPDS No. 42-0876).

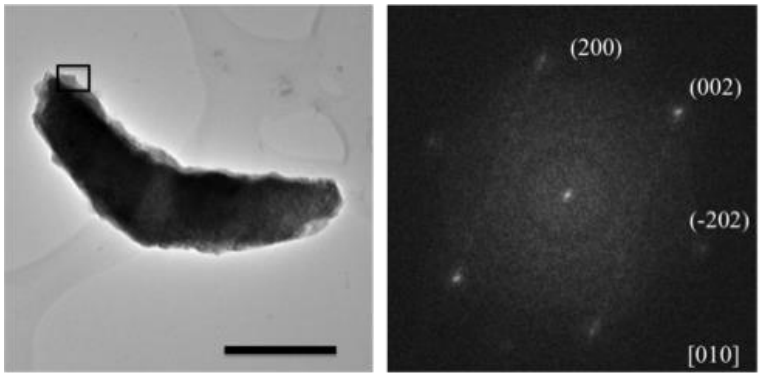


**Figure 3.8** Left: TEM image of a broken asterisk arm (scale bar: 500 nm). Right: SAED pattern collected from near the core (boxed area) matched to crystallographic data of $VO_2$(M). A diffraction pattern could not be obtained near the leading edge, indicating that it is amorphous.

precursor loading moving from $VO_2$-5mmol to $VO_2$-25mmol was associated with a decrease in the relative intensity of the (011) reflection of the $VO_2$(M) phase and an increase in the intensities of the (102) and (211) reflections of $VO_2$(A). These changes were likely related to the decreasing particle size and truncated asterisk arms observed by SEM for preparations at higher precursor loading. As shown in **Figure 3.8**, examination of a broken asterisk arm by SAED provides lattice d-spacing consistent with $VO_2$(M) with no contribution from $VO_2$(A) near the core, whereas at the leading edge, a diffraction pattern could not be obtained. This suggests that as the arms lengthen, the new atomic layers are amorphous in nature and crystallize over time to the intermediate $VO_2$(A) phase and finally to the $VO_2$(R) phase.

### *3.4 Particle Formation Mechanism*

To determine the formation mechanism of $VO_2$-20mmol particles, a time-resolved structure analysis was performed at time points ranging from 30 minutes to 24 hours, as shown in **Figure 3.9**. After 30 minutes of hydrothermal reaction time, the resulting product was isolated and identified after drying as $V_2O_4 \cdot 2H_2O$ (JCPDS No. 13-0346). At one hour, the product had changed to $V_{10}O_{24} \cdot 9H_2O$ (JCPDS No. 25-1006). Both products contained a wide variety of particle morphologies that had aggregated during the drying process. Interestingly, at the two-hour threshold, the observed particles had taken on a sharp ellipsoid shape (similar to that observed in the $VO_2$-25mmol particles) and some had begun exhibiting growth of the asterisk arms; this coincided with the emergence of $VO_2$(A) peaks in the pXRD spectrum. We attribute this evolution of morphology to an oriented attachment mechanism. At the eight-hour time point, there was observable growth of arms

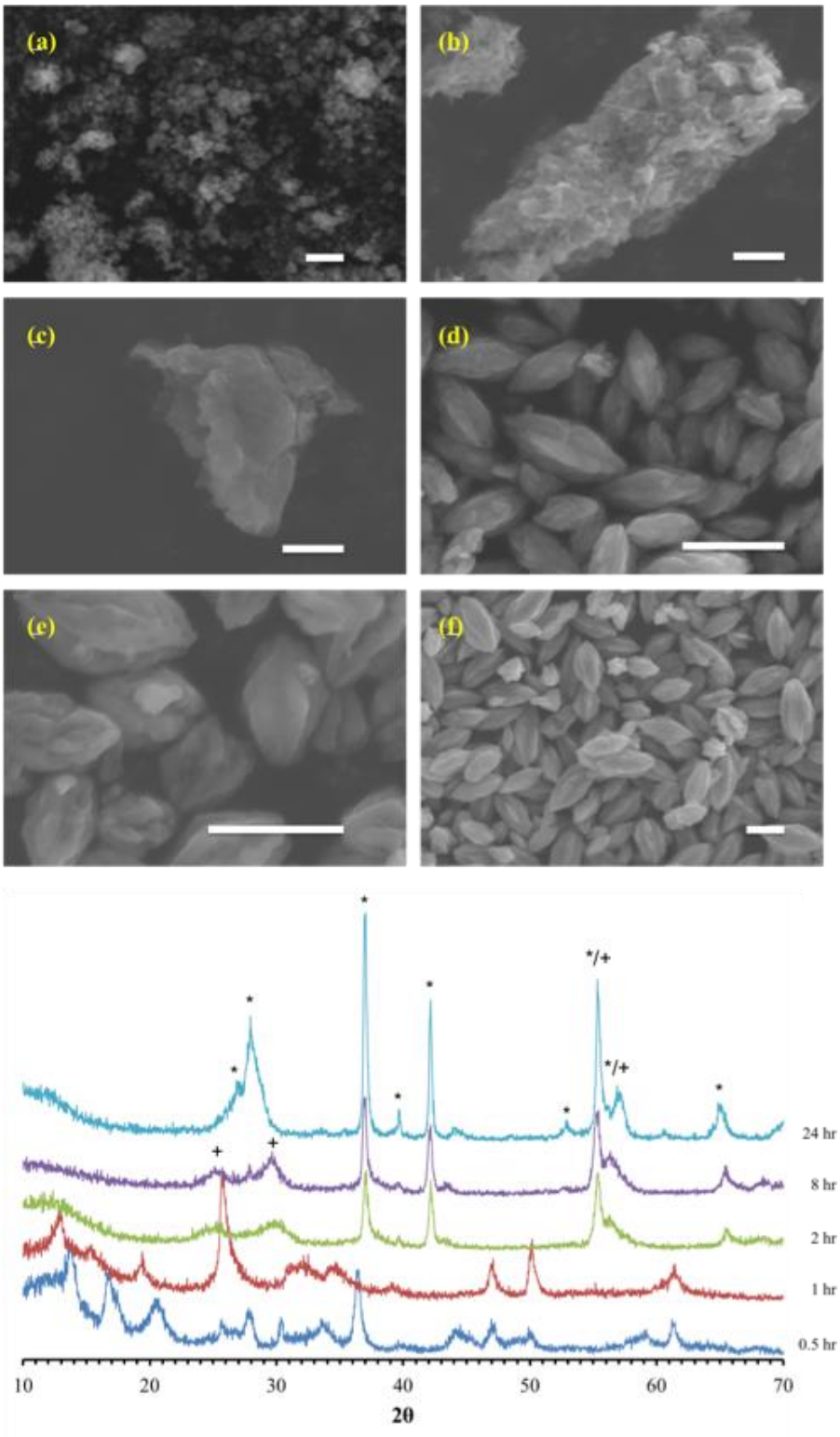


**Figure 3.9** Top: SEM images of (a) precursor material; (b) 30 minute time point; (c) 1 hour time point; (d) 2 hour time point; (e) 4 hour time point; and (f) 8 hour time point. Bottom: pXRD patterns obtained from various time points. Peaks associated with $VO_2$(M) are denoted by * and $VO_2$(A) peaks are denoted by +. Scale bars: 1 μm

on nearly all of the particles and the major (011) reflection of $VO_2$(M) was observed growing at 27.8º. By 24 hours, the (102) and (211) reflections of $VO_2$(A) have been overwhelmed by the (011) reflection of $VO_2$(M). Given the unique size and morphology of the $VO_2$-20mmol particles, $N_2$ adsorption-desorption was used to determine that the surface area was 4.1 $m^2$ $g^{-1}$, which was consistent with the particle shape and size.

### *3.5 Particle Film Characterization*

Film thickness was determined by stylus profilometry using a Veeco Dektak 150 Profilometer with a 12.5 μm radius tip, 8 mg applied force, and a resolution of 0.074 μm/tap. Prior to using the instrument, a single valley was carved into each film using a fine-tipped wooden rod. By setting the valley as the zero point, the average value obtained from the stylus on either side of the valley were averaged together and taken as the overall thickness. All films, regardless of particle size, were 3.6 ± 0.7 μm thick, corresponding to approximately 2–3 particle layers for the larger asterisks and 4–6 layers for the smaller asterisks. Based on the images in **Figure 3.3**, this was considered to be sufficient for achieving a contiguous film.

Initially, films of the $VO_2$ particles were analyzed by optical transmittance. Films of $VO_2$-10 mmol particles were prepared and their optical behavior was probed as a function of temperature. A comparison of the $VO_2$ particle film hysteresis behavior and a 120 nm thick $VO_2$ thin film is shown in **Figure 3.10**. The hysteresis width was approximately 15 K, which was expected based on the small size of the particles. What was most interesting about the particle film hysteresis curve was that it was the reverse of

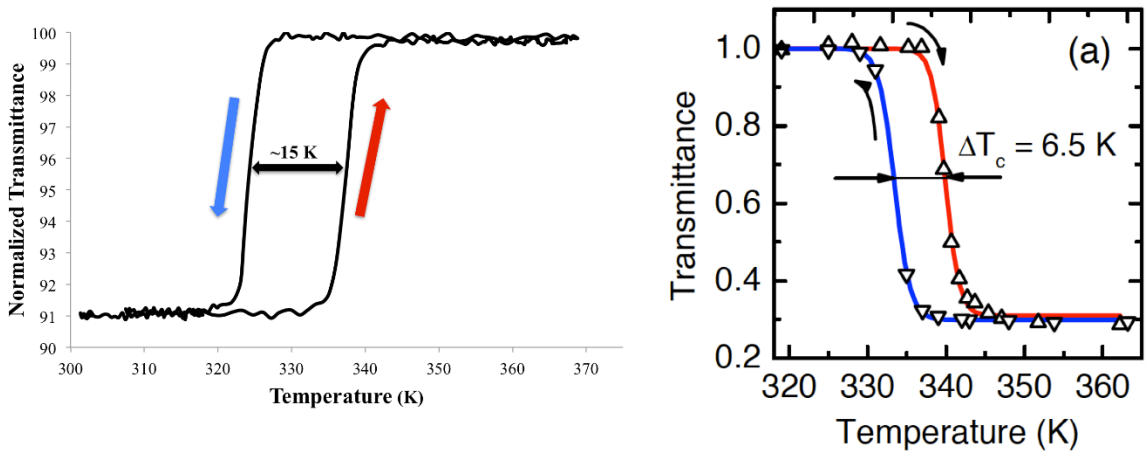


**Figure 3.10** Comparison of optical switching behavior between a $VO_2$ particle film (left) and a $VO_2$ thin film (right).[71] The switching temperature for the particle film was ~63ºC with a hysteresis width of ~12ºC.

what it should have been based on $VO_2$'s optical behavior; specifically, that the transmittance increases as a function of temperature rather than decreases. One possible contribution to this is that the film is made of discrete particles. In addition to the optical and electronic changes that occur at the SMT, there is also a density change (M: 4.571 g/cm$^3$, R: 4.653 g/cm$^3$), meaning that the particles must shrink in size when they convert to the rutile phase. This volume decrease, summed over the many particles that make up the film, would allow more light to pass through the film, resulting in an increase in transmittance. Another possibility is that we are observing the difference in how semiconducting and metallic $VO_2$ particles interact with light insofar as metallic particles tend to scatter light, which could explain the increase in observed transmittance. Due to the abnormalities observed with optical behavior, four-point resistivity was instead used for further film analyses.

Four-point van der Pauw resistivity measurements were used in order to determine the critical phase transition temperature, $T_c$, for the particle films. To date, resistivity measurements have focused on either thin films (<50 nm) of $VO_2$(M),[4,72,73] pressed pellets

of $VO_2$(M),[74,75] or on individual $VO_2$(M) particles.[76] Initial results revealed that when multiple scans were performed in succession on one film, the results for the overall resistivity and $T_c$ of the initial scan varied from the subsequent scans. We attribute this to the thermal expansion and contraction of the particles during the heating and cooling cycles. As $VO_2$(R) is more dense than $VO_2$(M), each particle should decrease slightly in size during the heating process; this could have interfered with the measurement, as the particles may have lost contact with one another. To minimize the impact of this on the measurements, each film was preheated to 100ºC for 5 minutes to allow for the complete conversion to $VO_2$(R), thus allowing the particles to settle. Upon cooling, the particles should expand during conversion to $VO_2$(M) to ensure better inter-particle contact. $T_c$ and hysteresis widths were determined by plotting the first derivative of the log of resistivity versus temperature and finding the local minima.

The resistivity of the particle films during a heating/cooling cycle is shown in **Figure 3.11**. $VO_2$-5mmol films did not exhibit a sharp phase transition, likely due to poor contact between the large particles. $VO_2$-10mmol films exhibited a $T_c$ of 345 ± 7 K with a hysteresis width of 6 ± 6 K and a resistivity change ($\Delta\rho$) of approximately one order of magnitude; $VO_2$-15mmol films exhibited a $T_c$ of 347 ± 5 K and a hysteresis width of 9 ±4 K. These were slightly higher than the bulk transition temperature for $VO_2$(M) of 341 K. This can be attributed to the fact that the mid-point transition temperature was used in determining $T_c$, however, the initial sharp drop occurred close to 341 K. Because the particles did not convert to the R phase at the same time, the change in resistivity took place over a wide temperature window of 5–15 K. $VO_2$-20mmol films exhibit a $T_c$ of 334± 2 K and a hysteresis width of 20 ± 2 K. These particle films also had the greatest $\Delta\rho$ of

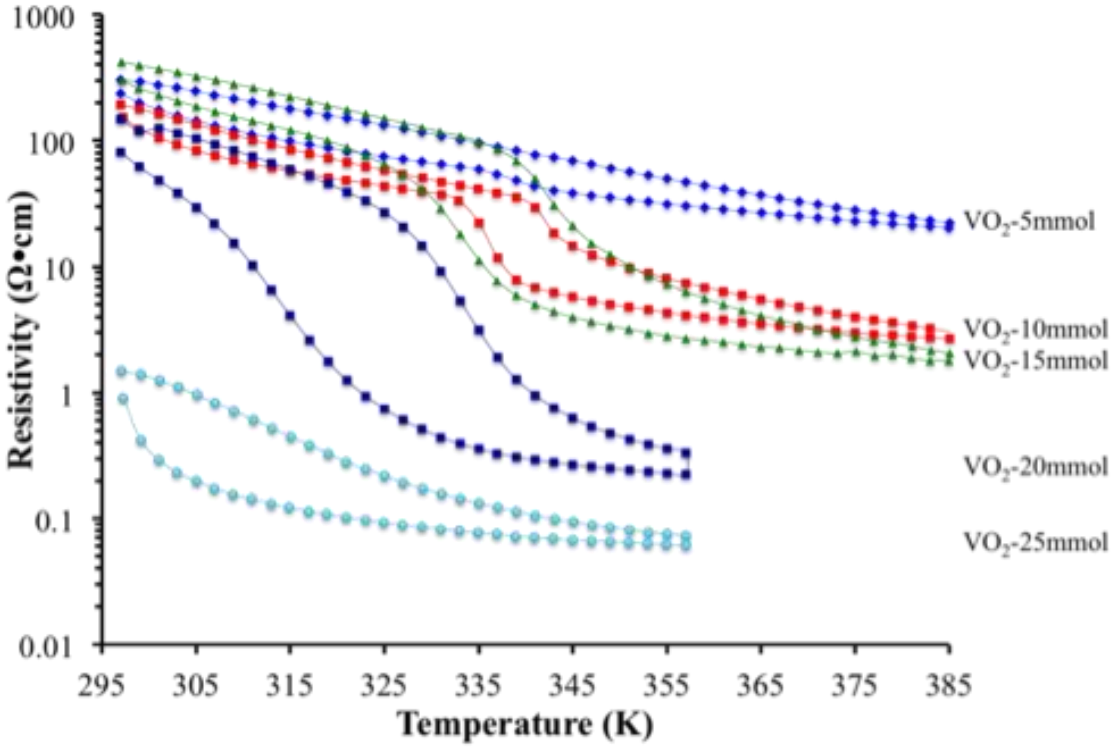


**Figure 3.11** Four-point van der Pauw resistivity measurements of $VO_2$ particle films deposited on thin glass substrate.

approximately two orders of magnitude, which was close to the three orders of magnitude previously reported for $VO_2$(M) thin films.[4,77]

The remarkable difference in the transition temperature between the $VO_2$-15mmol particles and $VO_2$-20mmol particles was unexpected since the particles were of similar size (see Section 3.3.2). However, the pXRD patterns offer an explanation in that the two sets of particles had very different crystallite sizes. In polycrystalline materials, the peaks observed in pXRD patterns can be broadened as a function of the size of the crystallographic domains. This relationship was established by Scherrer in 1918 and can be described by the equation

$$\tau = \frac{0.9\lambda}{\beta \cos\theta} \quad \textbf{(3.1)}$$

where $\lambda$ is the wavelength of the radiation, $\beta$ is the full width at half max (FWHM) of the peak being analyzed, and $\theta$ is the angle at which the peak is observed.[78,79] Using this equation, the crystallite sizes in the $VO_2$-15mmol and $VO_2$-20mmol particles were 32 nm and 15 nm, respectively. The decrease in $T_c$ observed with decreasing crystallite size was also consistent with previous studies of $VO_2$(M) nanoparticles.[5,80]

$VO_2$-25mmol films did not exhibit clearly defined switching, though the initial resistivity of the films was more than two orders of magnitude less than the other particle films. This was likely due, in part, to the presence of $VO_2$(A), which has a significantly smaller band gap than $VO_2$(M).[81]

### *3.6 Conclusions*

In conclusion, a series of $VO_2$ particles was synthesized by altering the amount of precursor present during hydrothermal treatment. This resulted in a variety of particle

morphologies and sizes. Additionally, an oriented attachment mechanism was proposed for the asterisk formation based on time-resolved structure analysis. For the first time, four-point van der Pauw resistivity measurements were made on drop-cast films of $VO_2$; these films exhibited a change in resistivity of up to two orders of magnitude. Therefore, films of these particles may find application as inexpensive, relatively high surface area electrodes with a readily accessible semiconductor-to-conductor transition.

CHAPTER IV

# VANADIUM DIOXIDE AS AN ELECTROCATALYST FOR THE DETECTION AND REDUCTION OF 2,4,6-TRINITROTOLUENE

## *4.1 Background*

The nitroaromatic compound 2,4,6-trinitrotoluene (TNT) has been widely utilized by the military and civil sectors as an explosive. The U.S. Army has estimated that at least 1.2 million tons of soil within the United States is contaminated by explosive compounds, mostly around munitions sites.[82] In addition to being explosive, TNT and its derivatives are also known to be mutagenic with long term exposure resulting in conditions such as aplastic anemia, toxic hepatitis, cataracts, hepatomegaly, and liver cancer.[83] The United States Environmental Protection Agency has set the maximum exposure limit of TNT in drinking water at 2 ppb,[84] necessitating the need to both detect and eliminate TNT from the environment in a rapid and cost-effective manner.[85,86]

Electrochemical methods have been shown to allow for rapid and sensitive detection of TNT and TNT derivatives.[87] In water, TNT is known to undergo three separate six-electron, six-proton transfers between –0.4V and –0.9V (vs. Ag/AgCl), corresponding to the successive reduction of each nitro group to an amine (**Figure 4.1**), resulting in the fully reduced 2,4,6-triaminotoluene (TAT).[88] Currently, ZnO[89] and $TiO_2$[90,91] nanoparticles are the only references to metal oxides being used as electrocatalysts for TNT reduction. Recently, Casey *et al.* showed that $VO_2$ thin films deposited on ITO-coated glass can detect TNT at concentrations as low as 1 ppb using adsorptive stripping voltammetry (AdSV).[13] The thin films were prepared by electron beam deposition as described by Marvel *et al.*

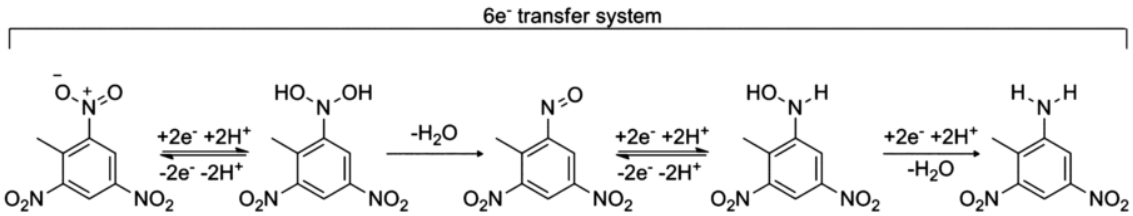


**Figure 4.1.** Reaction mechanism for the electrochemical reduction of one nitro group of TNT to an amine.[88]

and were approximately 60 nm thick.[92] Therefore, we hypothesize that coating an electrode with the previously synthesized $VO_2$ particles should yield improved results as compared to those seen in Casey's work due to increased surface area.

### *4.2 Methods & Materials*

Vanadium dioxide nanoparticles ($VO_2$-15mmol) were synthesized as described previously in Chapter III. A glassy carbon electrode (d = 3 mm) was polished using 0.5 μm alumina powder on a polishing wheel. $VO_2$ was anchored to the electrode by one of two methods. For the first method, the glassy carbon electrode was incubated in a 0.1% solution of poly-*d*-lysine for 15 minutes and any excess was wicked away. A 1.5 mg sample of $VO_2$ powder was suspended in 500 μL of deionized water and sonicated for at least two minutes to create a stable suspension. A 50 μL aliquot of the suspension was drop cast onto the electrode and dried in an oven at 100°C for at least 30 minutes (referred to as $VO_2$:PDL:GC). In the second method, a 1.5 mg sample of $VO_2$ powder was suspended in 500 μL of a 0.1% polyethyleneimine (PEI) solution and sonicated for at least two minutes. A 10 μL aliquot of the suspension was drop cast onto the electrode and dried in an oven at 100°C for at least 15 minutes (referred to as $VO_2$:PEI:GC). During this time, the reaction cell was assembled.

Twenty mL of 10 mM KCl was added to a 25 mL three-neck flask along with a stir bar. Ag/AgCl was used as the reference and Pt mesh served as the counter. All of the electrodes used were inserted into the flask through rubber septa to maintain a sealed environment. Once the $VO_2$-modified electrode was removed from the oven and cooled to room temperature, it was inserted into the flask. The reaction cell was then purged with medical grade nitrogen for at least 30 minutes and the gas flow was maintained during the subsequent electrochemical experiments to ensure complete expulsion of oxygen and prevent air from leaking back into the flask.

Electrochemical measurements were performed using a CH Instruments 660a electrochemical workstation. A 1000 ppm TNT standard in acetonitrile (Cerilliant, Round Rock, Texas) was used either directly or diluted in deionized water to make 100 or 10 ppm standards. For detections at low TNT concentrations (< 500 ppb), these standards were also sealed with rubber septa and purged with nitrogen to ensure no oxygen was being introduced to the system. Prior to any electrochemical experiments, the working electrode was cycled from 0.0 to -0.9 V for 25 cycles to remove any surface contaminants and establish a consistent background. Once the background was shown to be consistent, linear sweep voltammetry (LSV) was utilized to detect TNT during a titration. For extremely low TNT concentration calibrations, a preconditioning step was added whereby the working electrode was held at 0.0 V for 600 s under stirring to allow for TNT to adsorb to the $VO_2$ surface.

Raman spectroscopy data were collected using a Thermo Scientific DXR Confocal Raman Microscope equipped with a 532 nm laser. $VO_2$ samples were drop cast onto a Si substrate.

X-ray photoelectron spectroscopy (XPS) data were collected using a Physical Electronics (PHI) VersaProbe 5000 instrument. A 100 μm diameter monochromatic Al Kα x-ray beam (25 W, 15 kV) was rastered over an approximately 400 μm by 800 μm area. Electrons were collected at a takeoff angle of 45° off sample normal. Charge neutralization was accomplished using 1.1 eV electrons and 10 eV $Ar^+$ ions. Survey and high energy resolution spectra were acquired using pass energies of 187.85 eV and 23.5 eV, respectively. Energy scales were calibrated by placing the peak due to $-CH_2-$ type bonding in the C1s spectrum at 284.8 eV. Spectral analysis was performed using CasaXPS version 2.3.19 and handbook[93] sensitivity factors.

### *4.3 Surface Adsorption of TNT onto $VO_2$*

Glassy carbon is known to have some reactivity for the detection of TNT,[88–90] thus control experiment were performed, the results of which are shown in **Figure 4.2**. LSV was utilized to determine the reduction potentials of TNT on the $VO_2$:PDL:GC electrode. A background scan was performed before the addition of TNT for both glassy carbon and $VO_2$:PDL:GC electrodes; all data shown is background subtracted. Three reduction peaks, corresponding to the successive reduction of the three nitro groups can be seen at concentrations as low as 0.5 ppm. At 10 ppm TNT, the reduction potentials on the glassy carbon electrode were observed at –0.511 V, –0.687 V, and –0.819 V (**Figure 4.2a**). On the $VO_2$:PDL:GC electrode, the reduction peaks were observed at –0.503 V, –0.697 V, and –0.872 V (**Figure 4.2b**).

Casey *et al.* observed reduction potentials for 20 ppm TNT on $VO_2$ thin films at –0.542, –0.732, and –0.861 V vs Ag/AgCl and noted that, with increasing concentration,

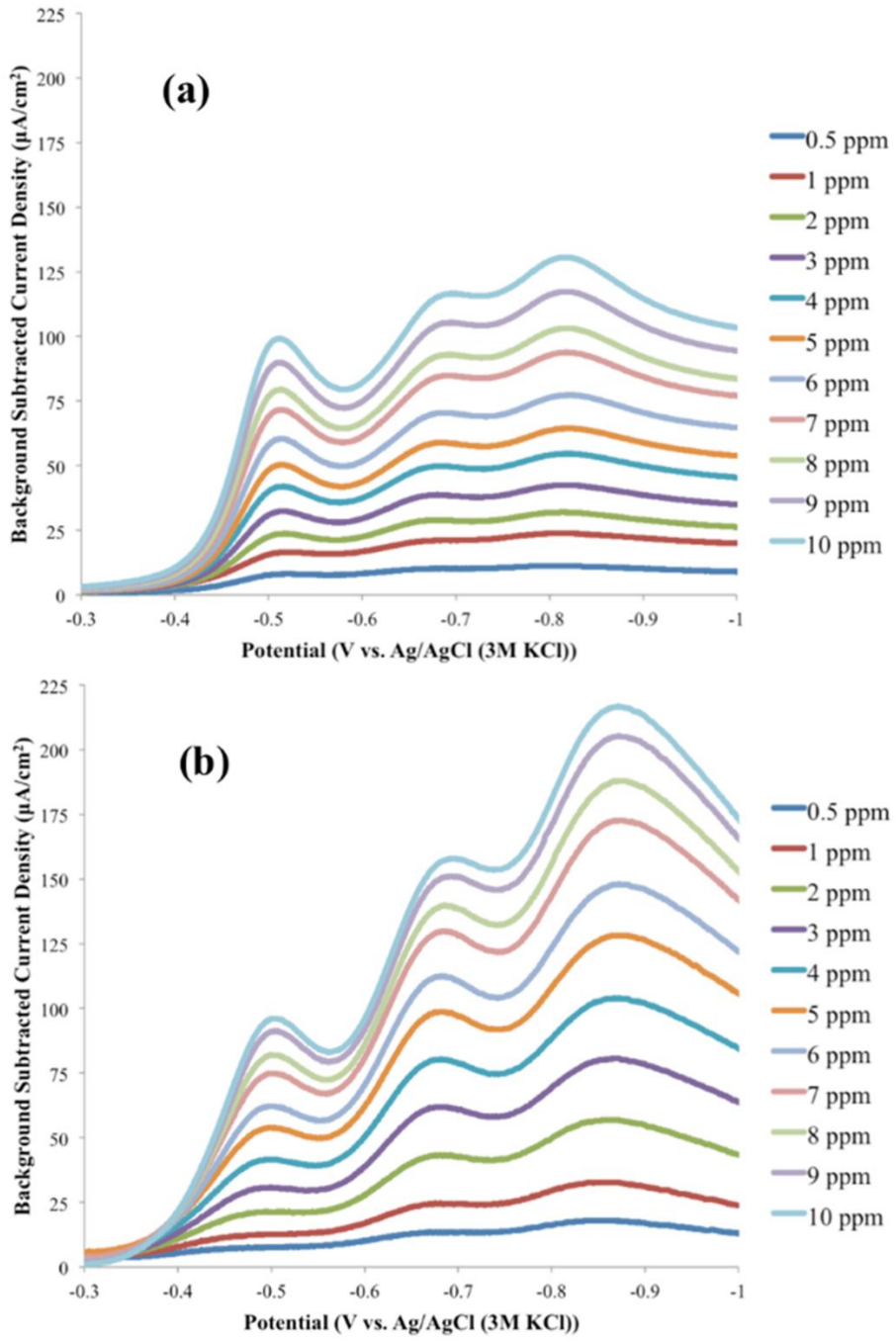


**Figure 4.2** Linear sweep voltammograms showing the three TNT reduction events at concentrations ranging from 0.5–10 ppm. Reduction potentials at 10 ppm TNT on glassy carbon (a) were observed at –0.511 V, –0.687 V, and –0.819 V, whereas reduction potentials at the same concentration on $VO_2$:PDL:GC (b) were observed at –0.503 V, –0.697 V, and –0.872 V.

the peak potentials shift to more negative potentials and become more broad.[13] The peak potentials observed on the $VO_2$:PDL:GC electrode occur at less negative potentials than on $VO_2$ thin films for the first two reduction peaks, shifting approximately 40 mV more positive. The third reduction peak shifts to a slightly more negative potential by approximately 10 mV. It is known that, for irreversible reduction reactions, the peak potential occurs at more negative potentials than the formal potential ($E^{0'}$) by an activation overpotential.[94] This activation overpotential is related to the heterogeneous rate constant, $k_0$. The relationship between the peak potential $E_p$, formal potential ($E^{0'}$), and heterogeneous rate constant ($k_0$) can be described by

$$E_p = E^{0'} - \frac{RT}{\alpha F}\left[0.780 + \ln\left(\frac{D_o^{1/2}}{k_0}\right) + \ln\left(\frac{\alpha F v}{RT}\right)^{1/2}\right] \qquad \textbf{(4.1)}$$

where $D_o$ ($cm^2\ s^{-1}$) is the TNT diffusion coefficient, $\alpha$ is the transfer coefficient, $v$ ($V\ s^{-1}$) is the scan rate, and $R$, $T$, and $F$ have their usual meanings.[94] Assuming that $\alpha = 0.5$ in both scenarios, the rate constant for the $VO_2$:PDL:GC electrode should be approximately five times larger than the $VO_2$ thin films. This is also consistent with the observation that, in general, the peaks observed with the $VO_2$:PDL:GC electrode do not shift to more negative values or broaden with increasing concentration, both of which would be indicative of slow reaction kinetics.

A calibration curve of the current density of the first reduction peak versus concentration of TNT (**Figure 4.3**) was prepared from the data shown in **Figure 4.2b**. There is a linear response observed from 0.5 ppm to 10 ppm. Interestingly, the $VO_2$:PDL:GC electrode shows only a slightly more sensitive response (10.07 ± 0.17 μA $cm^{-2}$ $ppm^{-1}$) than a glassy carbon electrode (9.22 ± 0.07 μA $cm^{-2}$ $ppm^{-1}$) for the first reduction peak. However, the $VO_2$:PDL:GC electrode was much more sensitive to the

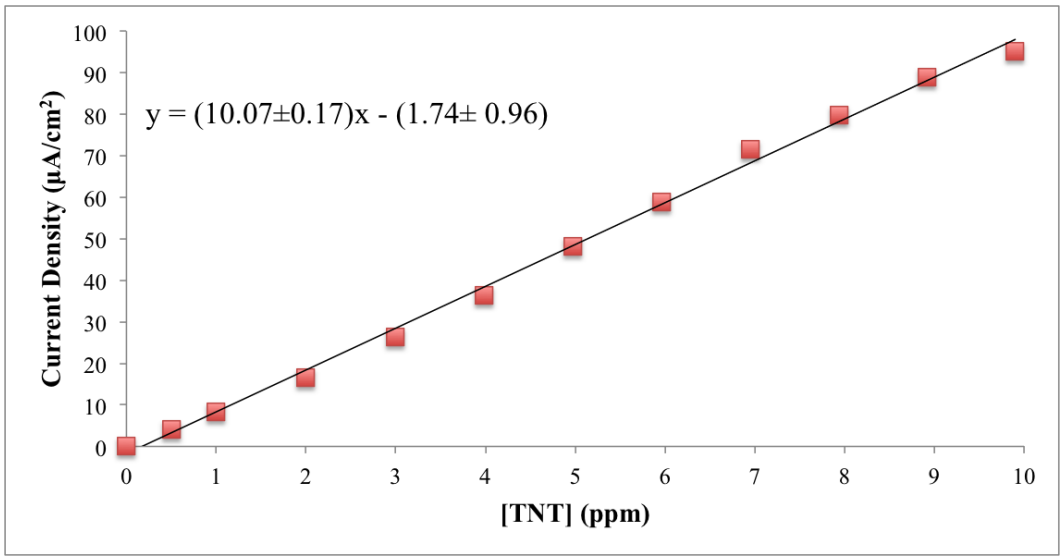


**Figure 4.3** Calibration curve of peak current density versus concentration of TNT using a $VO_2$:PDL:GC electrode with concentrations from 0.5 ppm to 10 ppm.

second and third reduction peaks, as can be seen in **Figure 4.2b**.

By modulating the scan rate, a distinction can be made between diffusion-limited and kinetically-limited processes. If a process is diffusion-limited, the peak current, $i_p$, will be proportional to $v^{1/2}$, which can be observed in the Randles-Sevcik equation

$$i_p = (2.69 \times 10^5) n^{3/2} A D^{1/2} C^* v^{1/2} \quad \textbf{(4.2)}$$

where $n$ is the number of electrons transferred per molecule, $A$ ($cm^2$) is the electrode area, and $C^*$ (mol $cm^{-3}$) is the bulk concentration of analyte. Conversely, when an analyte is not diffusion limited, it can be considered to be a surface-controlled reaction. In this scenario, the peak current is a function of surface coverage, $\Gamma$ (mol $cm^{-2}$), and scan rate, $v$, according to the equation

$$i_p = \frac{n^2 F^2 \Gamma A v}{4RT} \quad \textbf{(4.3)}^{95}$$

Thus, a plot of current vs. scan rate will be linear for a surface-controlled process and a plot of current vs. the square root of scan rate will be linear for a diffusion-limited process. However, this rule is not always perfect, as there are times when plotting against both scan

rate and its square root show linear regressions that are virtually indistinguishable from one another (similar $R^2$ value).

Measuring the peak current while varying the scan rate at a constant concentration of TNT revealed that the first reduction peak was a diffusion-controlled process (**Figure 4.4**). Typically, the second and third reduction peaks are not so well defined unless stripping voltammetry is utilized to encourage adsorption of TNT onto the electrode surface.[87] Measuring the peak current of the third reduction wave could not distinguish whether the process was a diffusion or surface controlled phenomenon. This could indicate that the reduction products (2-amino-4,6-dinitrotoluene (2A-DNT) or 2,4-diamino-6-nitrotoluene (2,4A-NT)) either adsorb to the surface of $VO_2$ or penetrate into the film and cannot readily diffuse out. This is further supported by the fact that, based on the peak current densities of the three reduction waves, when the concentration of TNT is low (< 2 ppm) essentially all of the TNT near the electrode surface is completely reduced to TAT ($i_{p,1} \approx i_{p,2} \approx i_{p,3}$). Under the same conditions and concentration, less than 20% of the TNT is completely reduced on a glassy carbon electrode (**Figure 4.2**).

To probe the adsorption of TNT onto the surface of $VO_2$ further, an experiment was set up to monitor the loss of TNT after the introduction of a known mass of $VO_2$ particles. In short, a TNT titration was performed using an unmodified glassy carbon electrode as described previously from 0.5 to 10 ppm. Once completed, 15.0 mg of $VO_2$ was introduced into the reaction cell and stirred from 15 minutes. Afterwards, the $VO_2$ particles were separated via centrifugation and the remaining supernatant was re-purged with nitrogen. The results of the experiment are shown in **Figure 4.5**. After mixing with the $VO_2$ particles, the concentration of TNT in solution decreased from 10 ppm to 5.8 ppm, which

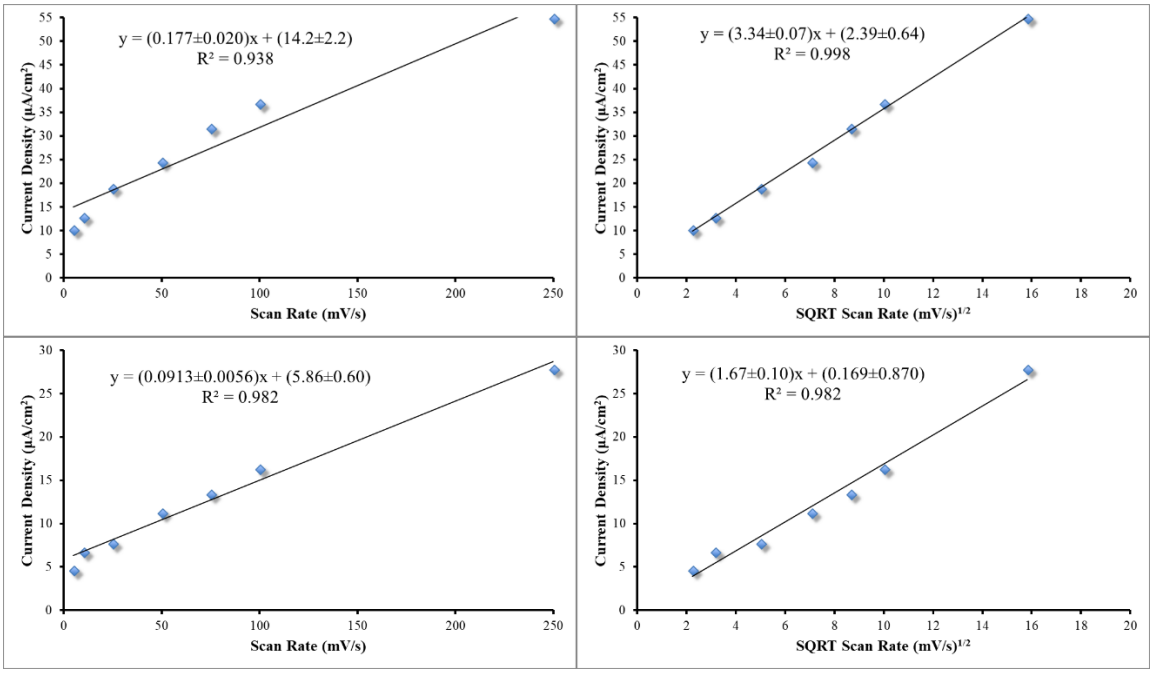


**Figure 4.4** Peak current for the first reduction wave using data from **Figure 4.2b** plotted against scan rate and the square root of scan rate (top) and peak current for the third reduction wave plotted against scan rate and square root of scan rate (bottom).

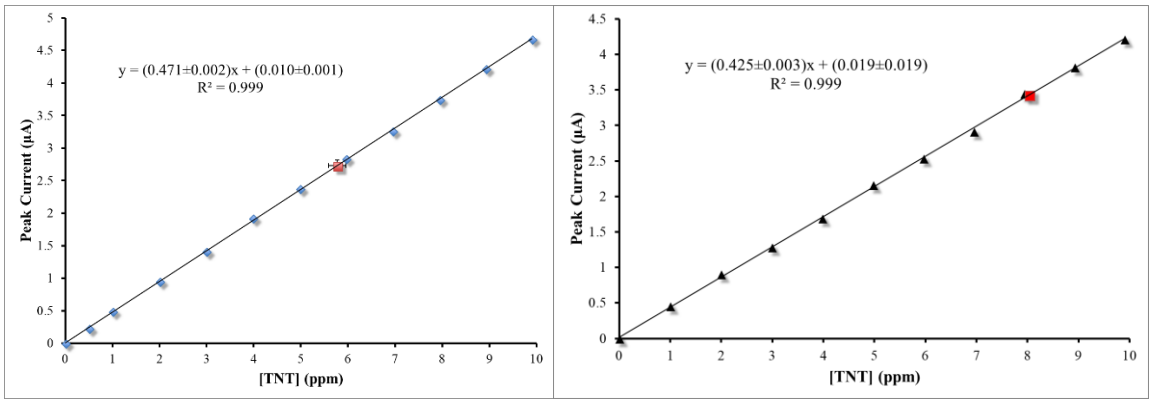


**Figure 4.5** Calibration curve of TNT titration using unmodified glassy carbon. The red square shows the current detected after the introduction of $VO_2$ particles (left) or $TiO_2$ particles (right).

corresponds to approximately 4 µg of TNT adsorbed per mg of $VO_2$. The $VO_2$ shows a superior adsorption to similarly sized $TiO_2$, which reduced the TNT concentration from 10 ppm to only 8.0 ppm. A similar experiment was repeated with a solution of 1 ppm TNT and, after introducing $VO_2$ particles, TNT was undetectable.

A likely explanation for the adsorption of TNT onto the surface of $VO_2$ is the presence of a large number of surface oxide vacancies. Surface oxide vacancies are, as the name implies, defects in which an oxygen is missing from the crystal lattice. These vacancies have been known to play a key role in other reactions such as the oxidation of CO to $CO_2$[96] or catalyzing the reduction of $CO_2$ to $CO_2^{\bullet-}$.[97,98] If one of the nitro groups of TNT is coordinating to an oxide vacancy, then it would explain why there is such a large enhancement in the 2nd and 3rd reduction peaks as compared to those observed when using bare glassy carbon.

### *4.4 Role of Surface Oxidation*

The surface chemistry of the $VO_2$ particles is extremely important in the detection of TNT. As mentioned in the previous section, it is likely that the presence of surface oxide

vacancies is crucial to the mechanism for the adsorption and subsequent reduction. However, other factors must be considered, as not every batch of $VO_2$ was capable of detecting TNT (even at ppm concentrations), even though there was no distinction when testing TNT adsorption. Two techniques were considered for probing the surface of the $VO_2$ particles: Raman spectroscopy and x-ray photoelectron spectroscopy (XPS).

Attempts at Raman spectroscopy were generally unsuccessful, even on the lowest laser power setting (1 mW). **Figure 4.6** shows a Raman spectrum obtained using 10 mW and 1 mW laser power compared to the spectra of a variety of vanadium oxides. The spectra obtained experimentally match very well with $V_2O_5$, regardless of the laser power used, indicating that the surface is being oxidized over the course of the measurement. This was also made apparent when the powder was viewed through the microscope and the area around the laser crosshairs was a bright yellow color (**Figure 4.7**), indicative of oxidation to $V_2O_5$.

XPS revealed slight differences in the surface oxidation states of samples that detect TNT and those that do not. Survey and high-resolution spectra of $VO_2$ can be seen in **Figure 4.8**, along with a breakdown of the corresponding atomic concentrations in **Table 4.1**. The vanadium near the surface was dominated by $V^{5+}$, likely a result of exposure to atmospheric oxygen; a small trace of $V^{3+}$ was also observed. A number of carbon bonding modes were also seen in the spectrum, which can be attributed to the ethanol used during the wash step after hydrothermal synthesis. One obvious difference between the two samples was the inclusion of a carbonyl mode in the sample that does not detect TNT; this mode does not appear in the other sample and there was no obvious source, as no carbonyl-containing compounds were involved in the synthesis or cleaning of the particles.

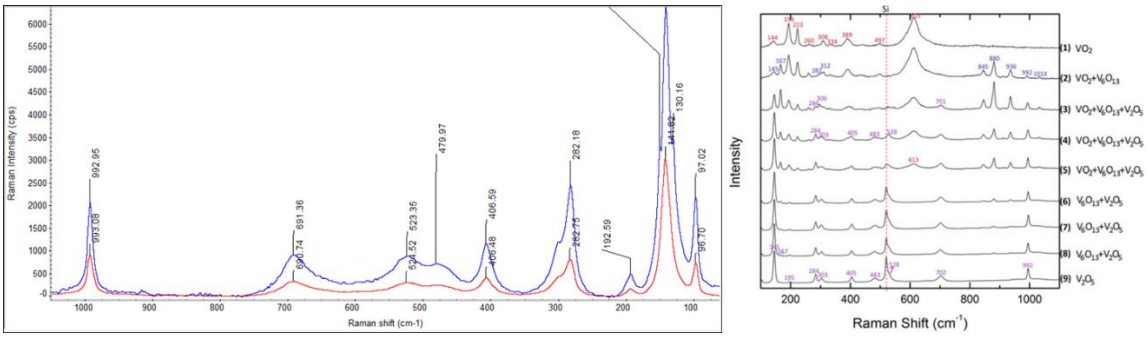


**Figure 4.6** (Left) Raman spectrum of $VO_2$ powder using 10 mW (blue) and 1 mW (red). (Right) Expected spectra of vanadium oxides.[99]

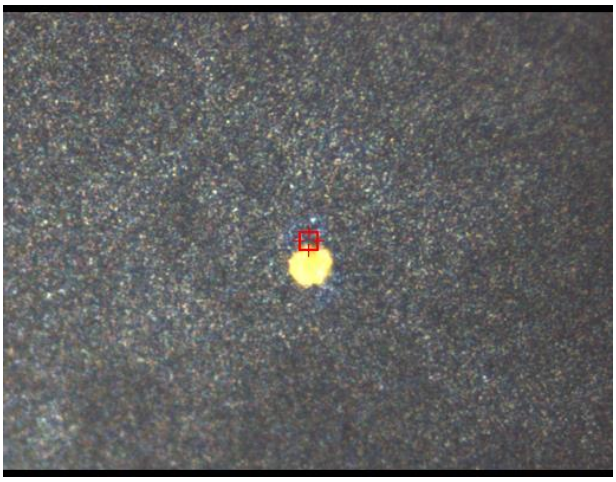

**Figure 4.7** $VO_2$ particle film after laser irradiation, revealing oxidation of the sample area.

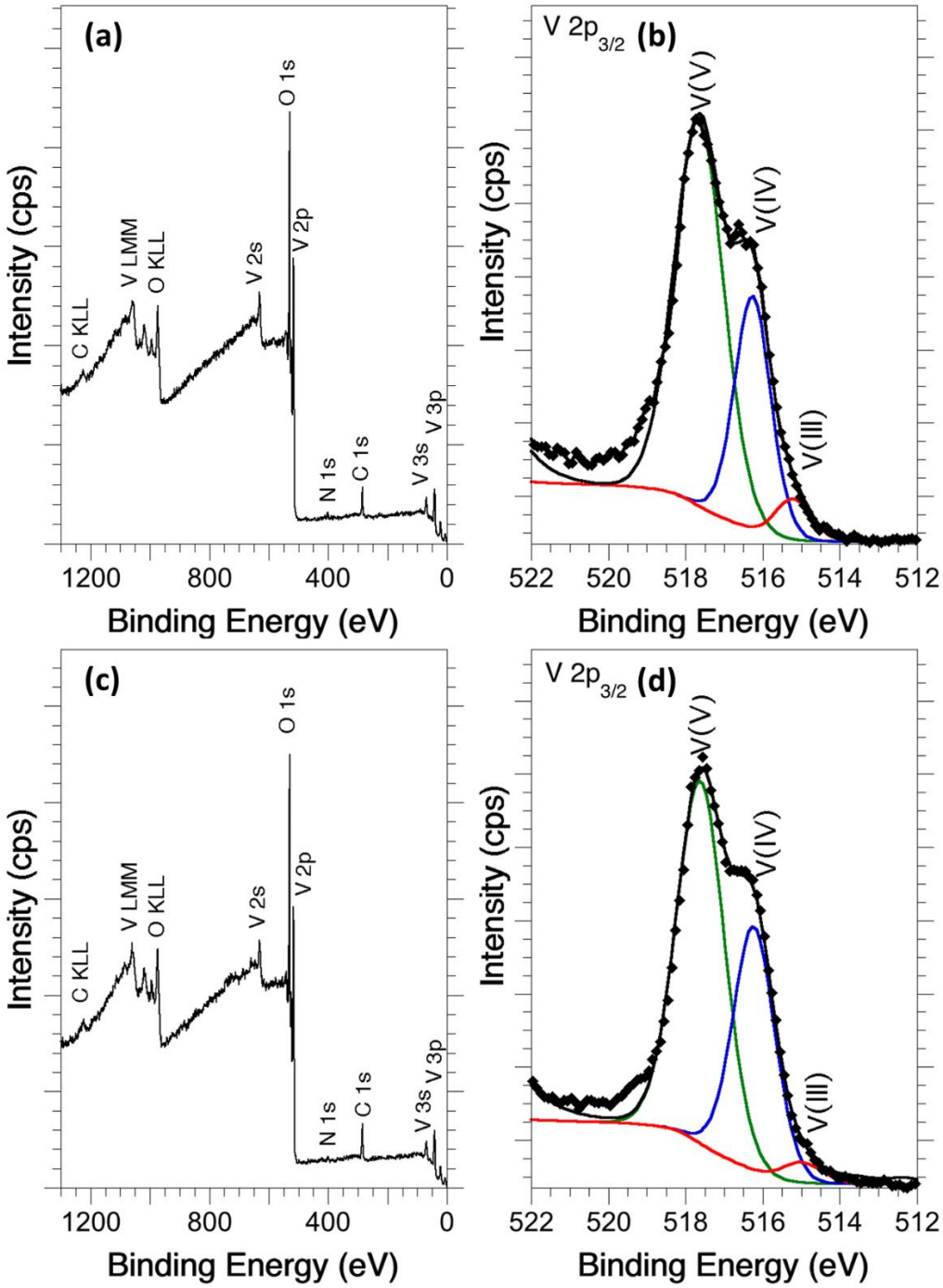


**Figure 4.8** XPS experimental data, fitted model and peak deconvolution for the vanadium oxide powders at different oxidation states. (a) and (b) represent data for a TNT-detecting $VO_2$ sample, (c) and (d) represent data for a sample that does not detect TNT.

**Table 4.1** Breakdown of XPS data from **Figure 4.8** showing atomic percentages obtained from peak deconvolution.

| Name | Position (eV) | Atomic % (No Detect) | Atomic % (Detect) |
|---|---|---|---|
| C-C, C-H | 284.8 | 32.6 | 31.4 |
| C-OH, C-O-C | 286.3 | 11.9 | 9.4 |
| O-C=O | 288.7 | 8.0 | 0.0 |
| V $2p_{3/2}$ V(V) | 517.6 | 26.7 | 35.6 |
| V $2p_{3/2}$ V(IV) | 516.2 | 15.7 | 15.8 |
| V $2p_{3/2}$ V(III) | 515.0 | 1.3 | 2.8 |
| N 1s $NH_3^+$ | 401.9 | 2.1 | 3.0 |
| N 1s $NH_2^+$ | 400.0 | 1.2 | 0.9 |
| N 1s N ring (organometallic) | 399.0 | 0.5 | 1.1 |

### *4.5 Detection of Low Concentration TNT*

The maximum allowable limit for contamination of TNT in drinking water is set at 2 ppb for prolonged exposure,[84] thus TNT must be detectable at this limit. Using a preconcentration step is a common method for improving the sensitivity and detection limit of a given analytical technique. In this case, a potential of 0.0 V was applied to the working electrode for 600 s under vigorous stirring to encourage TNT to collect on the $VO_2$ surface. Additionally, the $VO_2$:PEI:GC electrode was used in favor of the $VO_2$:PDL:GC electrode for these more sensitive tests. The PDL anchors the $VO_2$ to the electrode surface via electrostatics, as the surface of $VO_2$ is negatively charged. However, while the PDL worked well for experiments at high TNT concentrations, the inclusion of the electrostatic layer greatly increased the non-faradaic current. A background scan using a $VO_2$:PDL:GC electrode generally had currents in the $10^{-5}$ A regime. By switching to PEI, the background current was reduced by two orders of magnitude, making detection of small amounts of TNT possible. A TNT titration from 5 to 40 ppb is shown in **Figure 4.9**. A linear response

was observed over the tested range. However, when replicating the experiment, the response was not always linear, sometimes resembling a Michaelis-Menten curve. This implies that small variations in the mass of $VO_2$ on the surface can affect large changes in the observed response.

Attempts to detect TNT below 5 ppb were generally unsuccessful, despite having an increased surface area of $VO_2$ compared to the previous work that used thin films. This is counterintuitive, as one would expect that with increased surface area, the amount of TNT that can be collected during preconcentration would increase the signal. However, an additional consideration is the fact that, as a drop-cast film, the $VO_2$ particles create a very rough surface (in comparison to a thin film). This surface roughness increases the double-layer capacitance, which can be observed experimentally as an increase in non-faradaic current. This increase, as compared to the $VO_2$ thin films, was likely responsible for overpowering the small signal expected for sub 5 ppb TNT detection.

### *4.6 $VO_2$ Electrochemistry at Elevated Temperature*

The ability for $VO_2$ to switch from exhibiting semiconductor behavior to metallic behavior at elevated temperatures could result in interesting electrochemical behavior. To explore this, a reaction cell was prepared as described earlier. A cyclic voltammogram

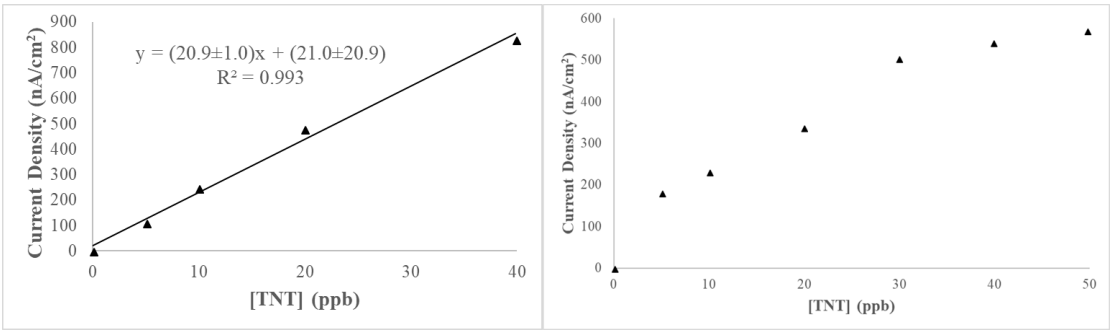


**Figure 4.9** Sample TNT titrations between 5 – 50 ppb. Responses may be linear (left) or exhibit Michaelis-Menten reaction kinetics (right).

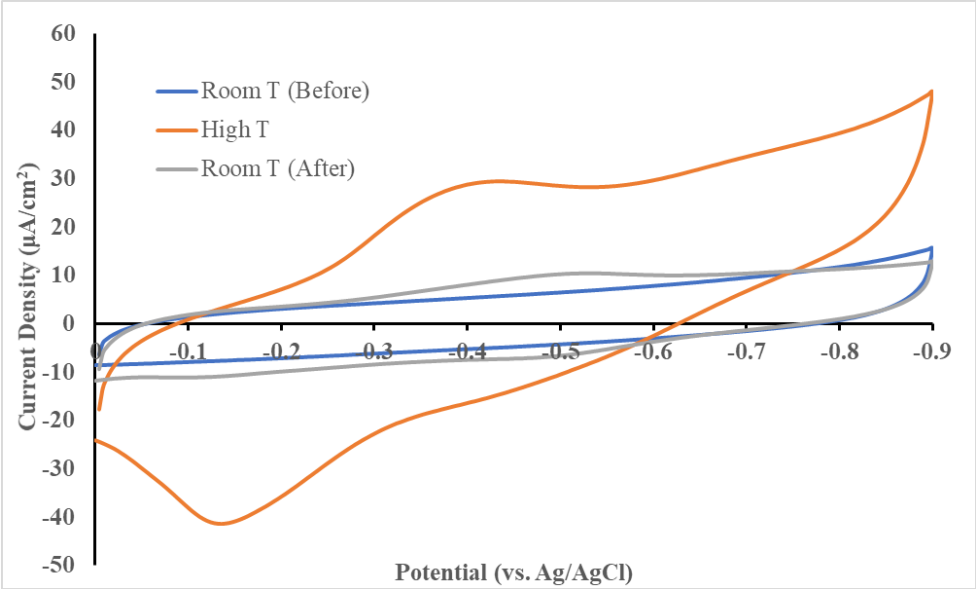


**Figure 4.10** Cyclic voltammograms of a $VO_2$-modified electrode in 10 mM KCl at room temperature and 75°C.

(CV) was obtained at room temperature, after which the entire cell was placed into a water bath at 75°C. This is well beyond the normal phase transition temperature, which ensured complete conversion of the $VO_2$(M) to $VO_2$(R). **Figure 4.10** shows a comparison of the cyclic voltammograms obtained at room temperature, at 75°C, and after cooling back to room temperature.

At room temperature, the CV of the $VO_2$-modified electrode was featureless in the relevant potential window. However, when heated, a redox couple appeared between -0.1 and -0.5 V with the reduction occurring at -0.382 V and the oxidation at -0.136 V. Based on those potentials, it is likely that this represents the $V^{3+}/V^{4+}$ redox couple.[100] The ratio of $i_{p,a}/i_{p,c}$ (anodic/cathodic peak currents) was 1.14 and $\Delta E$ (peak separation) was approximately 250 mV, indicating that this was a quasireversible reaction. After cooling back down to room temperature, the redox couple mostly disappeared. This can be

explained by the crystal distortions that occur during the phase transition. In the low temperature phase, the crystallographic planes exposed on the surface tend to be those dominated by oxygen. However, when the phase changes and the atoms reorient, the exposed planes become dominated by vanadium atoms. This was observed experimentally by Ji *et al.* when they measured the zeta potential of $VO_2$(M) nanorods as a function of temperature.[101] Their results revealed that at room temperature, the particles have an overall negative surface charge and, upon heating, gain an overall positive surface charge. Because the vanadium atoms are generally not exposed to solution at room temperature, the redox couple only appears when the $VO_2$ is in the R phase. However, since this redox couple occurs very close to the first reduction of TNT, it is likely that it will not be useful to perform TNT detections at elevated temperatures.

### *4.7 Conclusions*

Glassy carbon electrodes modified with vanadium dioxide nanoparticles were shown to be capable of detecting TNT reliably at concentrations as low as 5 ppb due in part to adsorption of TNT to the $VO_2$ surface. While this is still slightly above the EPA limit of 2 ppb, additional work may be able to push the detection limit below this threshold. Attempts to elucidate why some batches of $VO_2$ detect and others do not were met with inconclusive results. One possible reason is the presence of an unknown carbonyl-containing compound on the surface of particles that do not detect TNT. Additionally, the electrochemistry of the $VO_2$-modified electrodes was studied and revealed that the $V^{3+}/V^{4+}$ redox couple appears when it is in its high temperature phase due to changes surface-exposed crystal planes. The reduction of $V^{4+}$ to $V^{3+}$ occurs very close to the first reduction

of TNT, meaning that it would be difficult to decouple the signal obtained, especially when the TNT would be contributing only nanoamps of current.

### *4.8 Acknowledgements*

I would like to thank Prof. Bridget Rogers for her assistance in running and analyzing the XPS experiments. Also, thanks to Dr. Borislav Ivanov for his assistance with the Raman microscope.

# CHAPTER V

# TUNGSTEN DOPING OF $VO_2$ PARTICLES

## *5.1 Background*

As mentioned in Chapter I, the transition temperature of $VO_2$ can be either raised or lowered depending on the type and amount of dopant.[30] When sufficiently doped, the $VO_2$ can be forced into the high temperature metallic phase at room temperature. Because of its metallic nature, we hypothesized that the limit of detection for TNT would be improved compared to semiconductor $VO_2$ in part due to the lower resistance, which would decrease the background non-faradaic current.

## *5.2 Materials & Methods*

$VO_2$-20mmol particles were synthesized and characterized in a similar manner as in Chapter III, with minor modifications. After the precursor compound was synthesized, a known quantity of either ammonium paratungstate hydrate, $(NH_4)_{10}(H_2W_{12}O_{42})\cdot 4H_2O$, or sodium tungstate dihydrate, $Na_2WO_4\cdot 2H_2O$, was added during the stirring step and the hydrothermal reaction proceeded as normal. The precipitate was collected and washed with DI water and ethanol and dried at 100°C overnight. Samples with varying W-doping levels (1 at. %, 3 at. % 4 at. %) were prepared in this manner.

Electrochemical measurements were performed using a CH Instruments 660a electrochemical workstation. A 1000 ppm TNT standard in acetonitrile (Cerilliant, Round Rock, Texas) was used as the titrant. $VO_2$-modified electrodes were prepared as described

in Chapter IV using poly-*d*-lysine to anchor the $VO_2$ to the electrode surface. Twenty mL of 10 mM KCl was added to a 25 mL three-neck flask along with a stir bar. Ag/AgCl was used as the reference and Pt mesh served as the counter. All of the electrodes used were inserted into the flask through rubber septa to maintain a sealed environment. The reaction cell was then purged with medical grade nitrogen for at least 30 minutes.

### *5.3 Characterization*

SEM and TEM images of doped $V_{0.97}W_{0.03}O_2$ particles are shown in **Figure 5.1**. As compared to the $VO_2$-20mmol particles shown in Chapter III, the morphology is radically different, losing the distinctive asterisk shape and greatly decreasing in size, now

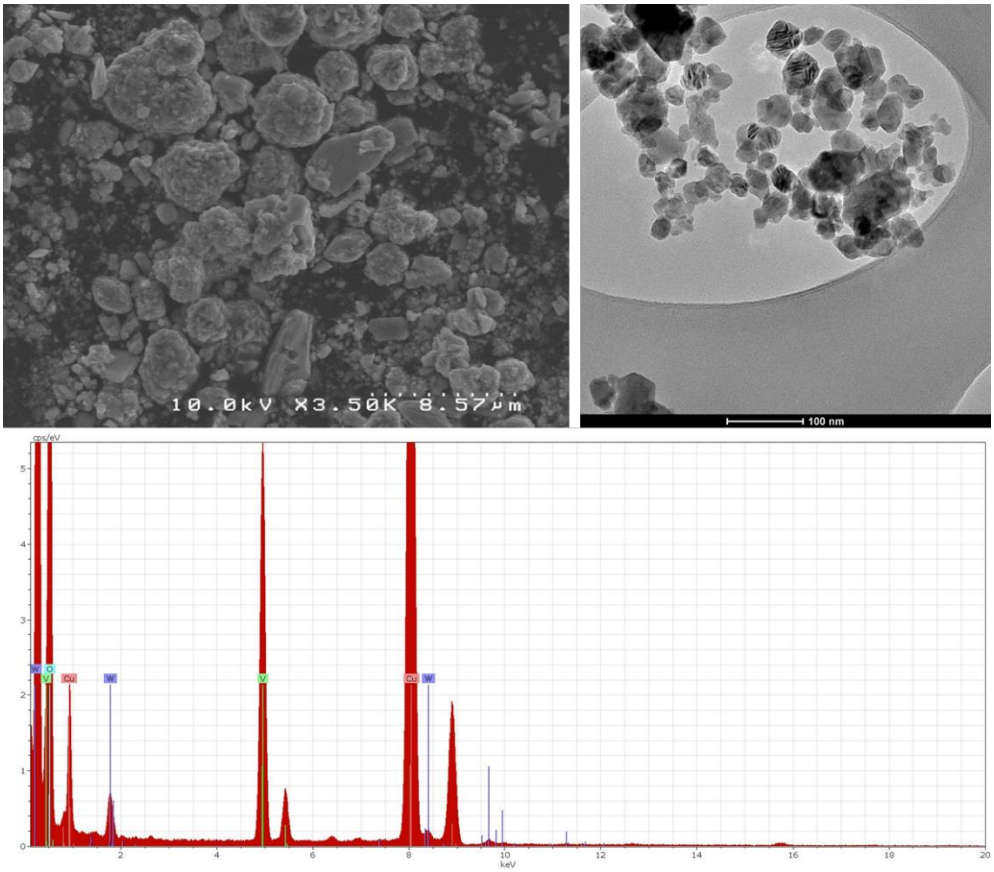


**Figure 5.1** SEM (top left) and TEM (top right) images of $V_{0.97}W_{0.03}O_2$ particles. The EDS spectrum (bottom) reveals the presence of tungsten.

in the range of 20-100 nm. This significant change is size may be attributed to an increase in oxygen vacancy density on the nanoparticle surface during crystal growth. Because $V^{4+}$ is of a lower oxidation state, the substitution of a $W^{6+}$ requires the presence of an oxide vacancy for charge compensation. This in turn presents a more positively charged surface, which may repel the diffusion of V monomer species and slow the growth of the particles.[102] The presence of tungsten in the sample was confirmed by energy-dispersive X-ray spectroscopy (EDS), which can identify elements based on the energy of X-rays emitted from the sample, which are unique to each element.

A comparison of the pXRD patterns of undoped $VO_2$ and doped $V_{0.97}W_{0.03}O_2$ is shown in **Figure 5.2** compared to the known patterns for $VO_2$(M) and $VO_2$(R), respectively. At 3 at. % W-doping, the phase transition temperature has been sufficiently suppressed that it matches with the pattern of $VO_2$(R) at room temperature. The absence of a phase transition can also be seen in a comparison of doped and undoped $VO_2$ samples

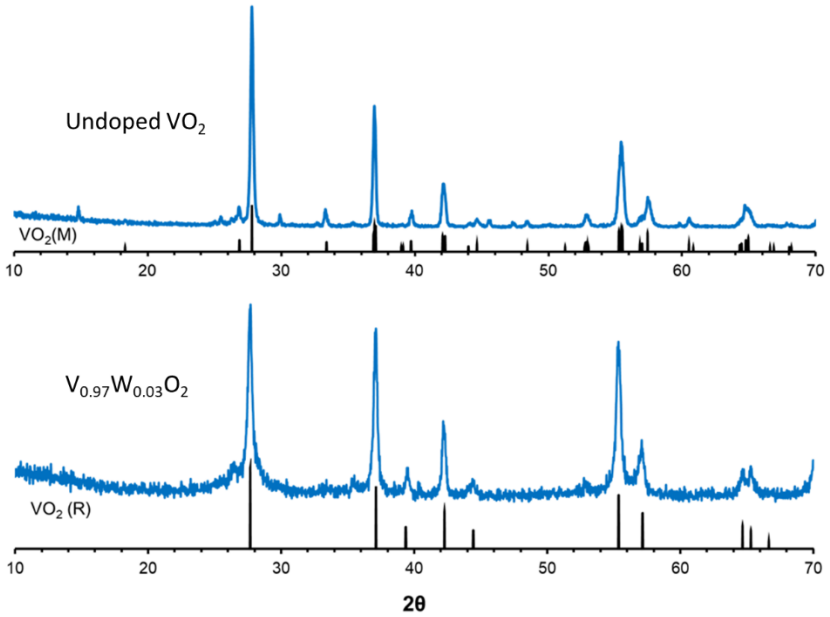


**Figure 5.2** Comparison of undoped $VO_2$ particles matched with the known XRD pattern of $VO_2$(M) (top) and particles doped with 3 atomic % W matched with the pattern of $VO_2$(R).

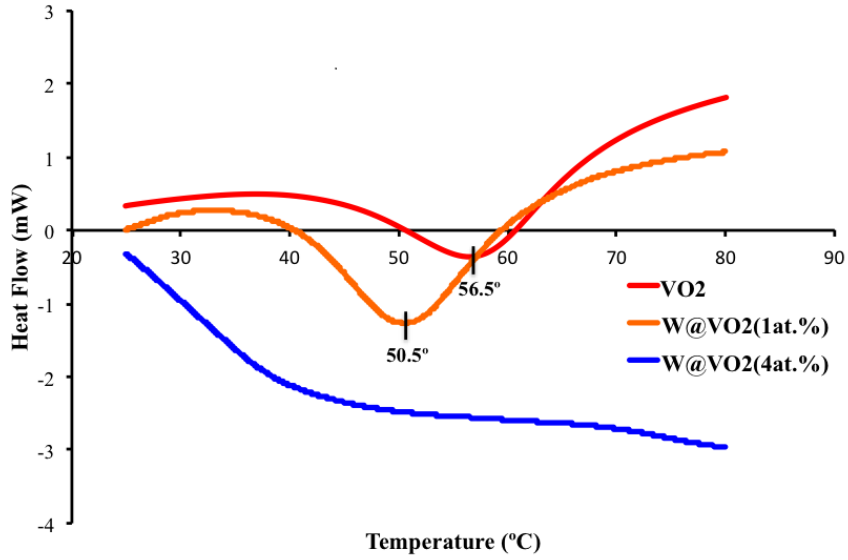


**Figure 5.3** Differential scanning calorimetry plots for undoped, 1 at. %, and 4 at. % doped $VO_2$ particles. No endothermic peak can be observed for heavily doped W:$VO_2$ particles, which indicates that there is no phase transition.

in differential scanning calorimetry, shown in **Figure 5.3**. The $V_{0.99}W_{0.01}O_2$ particles show a decreased transition temperature compared to the undoped $VO_2$ particles as expected. Four point resistivity measurements were also made on the doped particle films; however, due to their significantly smaller size, getting a contiguous film was extremely difficult due to the "coffee ring" effect.[103] The origin of this effect may be attributed to more rapid evaporation of solvent at the edges of a drop as compared to the center. This induces convection currents within the drop that drag small particulates towards the outer edge. Because the $V_{0.97}W_{0.03}O_2$ particles were so small, it was incredibly difficult to make a complete film, thus results from the four-point probe would be inaccurate.

### *5.4 TNT Detection & Solvent Effects*

Example TNT titrations using an undoped $VO_2$ and $V_{0.97}W_{0.03}O_2$-modified glassy carbon electrode are shown in **Figure 5.4**. The sensitivity of the doped electrode shows no

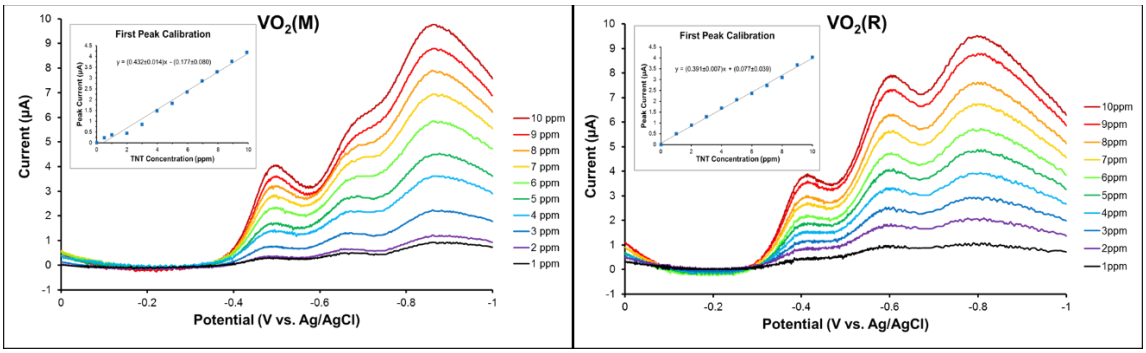


**Figure 5.4** TNT titrations using undoped (left) and 3 at. % doped (right) $VO_2$-modified glassy carbon electrodes.

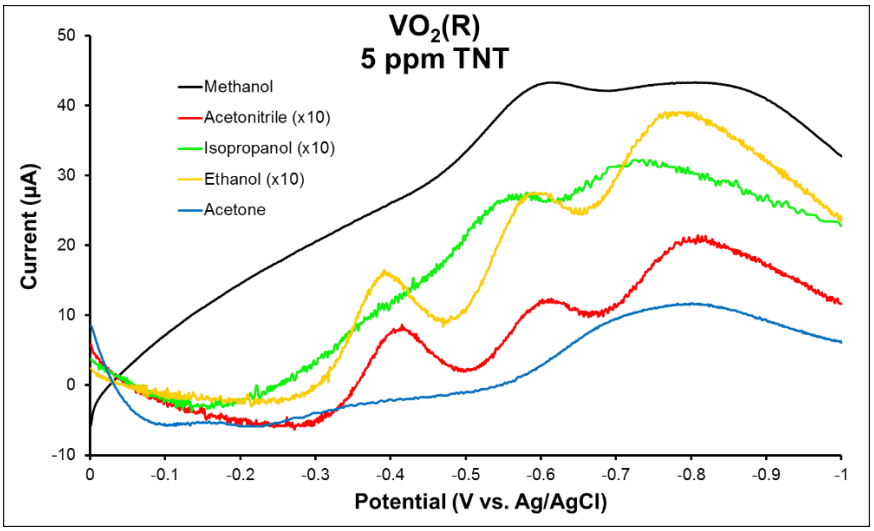


**Figure 5.5** LSVs of TNT detection using $V_{0.97}W_{0.03}O_2$ washed with various polar organic solvents.

significant enhancement over the undoped $VO_2$, shown by the similarity in the slopes of the calibration curves. However, over the course of the synthesis and experiments, an important discovery was made with regards to $VO_2$'s ability to enhance TNT detection. The identity of the organic solvent used during the wash step can inhibit the TNT sensing capabilities of $VO_2$, which is was especially apparent in the doped particles. A comparison of LSVs obtained at 5 ppm TNT between doped particles washed with a variety of polar organic solvents is shown in **Figure 5.5**.

Particles washed with acetone, methanol, and isopropanol show a drastic change in the LSV with acetone-washed particles losing all TNT detection capability. Methanol- and isopropanol-washed particles still seem to show some amount of detection, though only one or two peaks can be observed shifted several hundred mV more negative. This may be due to interactions of the solvent molecules with the surface oxide vacancies, which are likely responsible for the adsorption of TNT to the surface. If these sites are blocked, TNT adsorption may not occur. Additionally, as was apparent in the case of isopropanol, the solvent may react with the particles in a detrimental way. When mixed with isopropanol, the particles degrade, indicated by the supernatant turning green. This could be a result of the reduction of the surface vanadium to $V^{3+}$ (green in solution) or the release of $V^{4+}$ and $V^{5+}$ (blue and yellow in solution, respectively).

### *5.5 Conclusions*

Tungsten-doped vanadium dioxide nanoparticles were successfully synthesized and, at sufficient doping levels, existed as the high-temperature rutile phase at room temperature. These particles were then used to detect TNT, though they did not show

significant enhancement over undoped $VO_2$. However, over the course of the experiments, solvent effects were observed that interfered with the detection of TNT, especially acetone. This may be due to the solvent molecules blocking the surface oxide vacancies that, as discussed in Chapter IV, may be responsible for the TNT/$VO_2$ interactions.

### *5.6 Acknowledgements*

I would like to thank Jennifer Lomaki, who was responsible for collecting much of the preliminary data for the tungsten doping experiments. Also, thanks to Dr. Borislav Ivanov for his assistance with the DSC.

# CHAPTER VI

# CONCLUSIONS AND OUTLOOK

## *6.1 Summary*

The experiments presented in this dissertation have explored the synthesis of vanadium dioxide nanoparticles and their uses in electrochemical detectors for environmental contaminants. In Chapter I, the history of vanadium dioxide and how our understanding of its semiconductor-to-metal transition has evolved was discussed, as well as how the potential chemical applications for this material have been mostly overlooked compared to other transition metal oxides. In Chapter II, we briefly looked at some of the methods used to characterize $VO_2$ and expanded on the methods of four-point resistivity and differential scanning calorimetry.

In Chapter III, we showed that phase-changing vanadium dioxide nanoparticles can be synthesized hydrothermally, in relatively large quantities, and without the need for additional annealing steps. The phase of the final product, as well as its morphology, are greatly influenced by the fill fraction, presence of hydrazine, and precursor concentration. A time-resolved x-ray diffraction study revealed that the formation mechanism that our particles undergo is different from those previously reported for syntheses of this type and can be described as an oriented attachment. We also report, for the first time, the four-point resistivity of a $VO_2$ nanoparticle film, showing resistivity changes of up to two orders of magnitude.

Furthermore, in Chapter IV, we demonstrated the usefulness of $VO_2$ in the remediation of TNT in the environment. TNT readily adsorbs to the surface of $VO_2$, likely a result of coordination of the nitro groups to oxide vacancies on the surface. This adsorption allows for the complete reduction of TNT to TAT, which is typically not observed when using other electrodes. The surface chemistry of the material was probed using XPS to determine why there is variability in whether a particular batch of $VO_2$ particles will detect TNT, though the results were inconclusive. Using preconcentration strategies, TNT could be detected at concentrations as low at 5 ppb. Though this is higher than the EPA's target of 2 ppb, further work, including optimization of $VO_2$ loading and exploring more sensitive electrochemical techniques such as square wave voltammetry, could push this detection limit down even further.

Chapter V discussed the doping of $VO_2$ particles with $W^{6+}$ in an effort to make $VO_2$ particles that exist in the high-temperature R phase at ambient temperature. At 3 at. % doping, the XRD pattern matches with that of $VO_2$(R) and DSC revealed that there is no observable phase transition between 20°C and 100°C. The W-doped particles showed no significant enhancement in TNT detection, though solvent effects were observed that indicated blocking of active sites by solvent molecules.

### *6.2 Future Outlook*

This dissertation has focused mainly on the collective transition of the $VO_2$ particles as films; however, details about the phase transition of individual nanoparticles could provide new insights. Scattering-scanning near-field optical microscopy (s-SNOM) is a technique that can probe surface details smaller the Abbe diffraction limit ($\lambda/2$). In

combination with polarized far-field optical microscopy, s-SNOM has been used previously to observe unique striped semiconductor and metallic domains in single crystalline $VO_2$ nanorods.[104] The asterisk structure of the $VO_2$ described in this dissertation may reveal interesting patterns during an individual particle's phase transition.

While TNT is one of the most common and widely used nitroaromatic explosive compounds, it is by no means the only one. Other TNT derivatives—2,4-dintrotoluene (DNT) and 2,4,6-trinitrophenol (picric acid)—are also used, as well as newer and more powerful explosives like 1,3,5-trinitro-1,3,5-triazinane (RDX). How these compounds interact with the $VO_2$ surface as compared to TNT may be of interest, especially RDX considering that it is nonaromatic. Additionally, tests of water samples collected from rivers near construction or munitions test sites will be required to determine our system's applicability to real world samples.

Preliminary results showed that there is a significant change in the cyclic voltammogram for $CO_2$ reduction between a pure carbon paste electrode and one containing $VO_2$. Further testing via electrolysis will be needed to determine the actual products of the reaction and how overpotential affects the products and overall efficiency. After running electrolysis, an extraction of the catholyte into an organic solvent will allow for various tests to be run, including GC-MS and $^1$H NMR to determine the identities of any products. Additionally, in an effort to improve efficiency, polyethyleneimine can be added to the paste surface. Polyethyleneimine is known as a $CO_2$ absorbent and has been shown to serve as a co-catalyst for $CO_2$ reduction by lowering the catalytic overpotential.[105]

APPENDIX I

# VANADIUM DIOXIDE AS A CATALYST FOR ELECTROCHEMICAL CARBON DIOXIDE REDUCTION

## *A1.1 Background*

In recent years, concerns about the environmental impact of increasing $CO_2$ levels in the atmosphere and its contribution to global warming and the greenhouse effect has led to research in how to either sequester the gas underground or upgrade it into valuable fuels or feedstock chemicals.[106] The electrochemical reduction of $CO_2$ on various metal electrode surfaces has been a heavily researched topic for many years.[107–109] Depending on the metal, pH, and electrolyte, different products can be formed including carbon monoxide and many lower hydrocarbons, alcohols, aldehydes, ketones, and carboxylic acids.[110] A selection of relevant electrochemical reactions and their theoretical formation potentials is shown in **Table A1.1**.[108]

Oxygen vacancies on the surface of metal oxides such as $CeO_2$ and $TiO_2$ have been shown to be critical in the oxidation of CO to $CO_2$.[96,111,112] Previous work in the Cliffel lab has dealt with the capability of $V_2O_4$-supported Au nanoparticles to oxidize CO (with mixed results).[113] Oxygen vacancies are also known to catalyze the reduction of $CO_2$ to $CO_2^{\bullet-}$, the rate-limiting step of most $CO_2$ reduction mechanisms due to its extremely unfavorable thermodynamics and kinetics.[97,98] Reports of using metal oxide electrodes for aqueous phase $CO_2$ electro-reduction are limited, though $CoO_2$,[114] NiO,[115] CuO,[116] and $RuO_x/IrO_x$[117] have been used.

**Table A1.1** Theoretical reduction potentials for select $CO_2$ reduction reactions. All potentials (vs. Ag/AgCl) calculated under the assumption of pH = 7, 25°C, and atmospheric pressure.

| Reaction | Potential |
|---|---|
| $CO_2 + e^- \rightarrow CO_2^-$ | (-2.10 V) |
| $CO_2 + H_2O + 2e^- \rightarrow CO + 2OH^-$ | (-0.73 V) |
| $CO_2 + 6H_2O + 8e^- \rightarrow CH_4 + 8OH^-$ | (-0.46 V) |
| $2CO_2 + 8H_2O + 12e^- \rightarrow C_2H_4 + 12OH^-$ | (-0.55 V) |
| $2CO_2 + 9H_2O + 12e^- \rightarrow C_2H_5OH + 12OH^-$ | (-0.54 V) |
| $3CO_2 + 13H_2O + 18e^- \rightarrow C_3H_7OH + 18OH^-$ | (-0.53 V) |

The concentration of $CO_{2(g)}$, $HCO_3^-{}_{(aq)}$, and $CO_3^{2-}{}_{(aq)}$, in a solution can be estimated from a Bjerrum plot, assuming that the total dissolved inorganic carbon (DIC) and the pH are known.[118] Carbonic acid is formed by the reaction of $CO_2$ with $H_2O$, however it is unstable and will either dissociate back into $CO_2$ and $H_2O$ or undergo successive deprotonations into bicarbonate and carbonate. An example of a carbonic acid Bjerrum plot is shown in **Figure A1.1**. The concentrations of each species at equilibrium can be calculated using the equations

$$\left[CO_{2(aq)}\right] = \frac{[H^+]_{eq}^2}{[H^+]_{eq}^2 + K_{a_1}[H^+]_{eq} + K_{a_1}K_{a_2}} \quad \text{(A1.1)}$$

$$\left[HCO_{3(aq)}^-\right] = \frac{K_{a_1}[H^+]_{eq}}{[H^+]_{eq}^2 + K_{a_1}[H^+]_{eq} + K_{a_1}K_{a_2}} \quad \text{(A1.2)}$$

$$\left[CO_{3(aq)}^{2-}\right] = \frac{K_{a_1}K_{a_2}}{[H^+]_{eq}^2 + K_{a_1}[H^+]_{eq} + K_{a_1}K_{a_2}} \quad \text{(A1.3)}$$

where $pK_{a1}$ = 6.3, $pK_{a2}$ = 10.3, and $[H^+]$ can be determined from pH. For a $N_2$-saturated solution, the DIC is simply the molarity of the bicarbonate. However, for a $CO_2$-saturated solution, the solubility of $CO_2$ must be taken into consideration, which, at 1 atm of pressure,

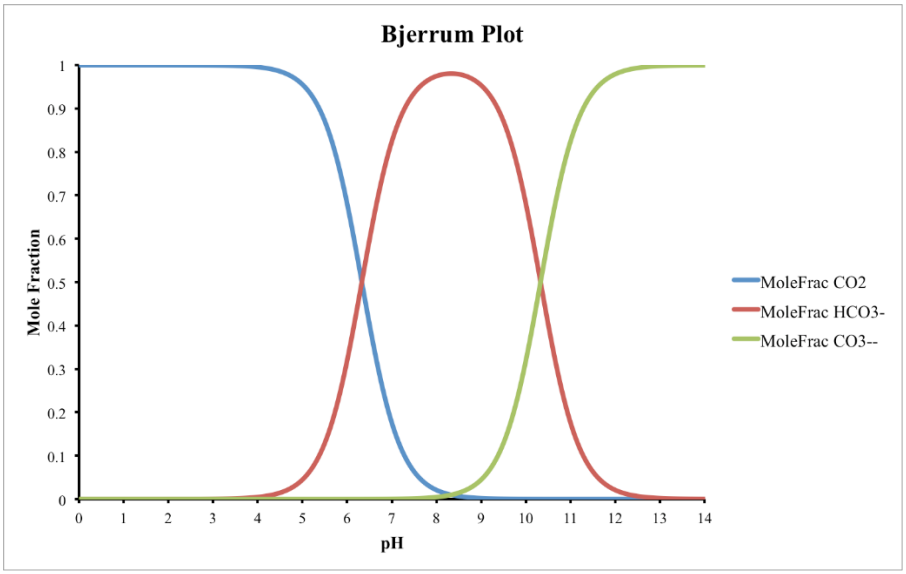


**Figure A1.1** Bjerrum plot showing the mole fraction of the dissolved inorganic carbon species at various pH values.

is equal to 34 mM (according to Henry's Law).[119] In this work, we examine the capability of $VO_2$ to catalyze the electroreduction of $CO_2$.

### *A1.2 Methods & Materials*

Vanadium dioxide nanoparticles ($VO_2$-20mmol) were synthesized as described in Chapter III. Unlike the TNT detection experiments, carbon paste electrodes (CPEs) were utilized, which were made by filling a hollow electrode body with a prepared $VO_2$-modified paste. The paste was prepared in a 35:(65-*x*):*x* ratio (by mass) of light mineral oil:graphite powder:$VO_2$ and tightly packed into the hollow electrode to ensure good contact with the interior electrical lead.

All electrochemical measurements were performed using a CH Instruments 660a electrochemical workstation. In a typical electrolysis experiment, a standard H-cell was utilized, which separates the anode and cathode between an ion exchange membrane. A platinum mesh electrode was used as the counter and was placed in the anolyte

compartment. Ag/AgCl was used as the reference and was placed in the catholyte compartment along with the $VO_2$-modified CPE. 0.1-0.5 M $NaHCO_3$ was used as the electrolyte and was purged with either $CO_2$ or $N_2$ for at least 30 minutes prior to experiments. Before electrolysis, cyclic voltammetry was used to determine an appropriate potential at which to hold the electrode. Cyclic voltammograms were recorded at $v = 0.1$ V $s^{-1}$. For electrolysis experiments, the working electrode was held at an appropriate potential for two hours.

### *A1.3 Results*

A series of CPEs were made using a variety of graphite:mineral oil content to determine which combination provided good electrical conductivity and packed well. Electrodes fabricated using 35% by mass of light mineral oil produced the cleanest electrochemical signals. Furthermore, two methods were used by which to incorporate $VO_2$ into the electrode. First, a prepared CPE was pressed into a sample of $VO_2$ to impregnate the powder into the surface; however, this led to difficulties in reproducibility and significant waste of $VO_2$ sample. Alternatively, the $VO_2$ powder was mixed directly in with the carbon powder during electrode fabrication. This provided greater control of the $VO_2$ content and more consistent results. Electrodes with $VO_2$ content greater than 25% were not mechanically stable and would disintegrate when submerged.

Cyclic voltammetry was utilized to determine the onset potential of reduction events in $CO_2$-purged 0.1 M $NaHCO_3$ (**Figure A1.2**). The carbon paste electrode, when cycled from 0.5 V to -2.5 V (vs. Ag/AgCl), showed an irreversible reduction event starting

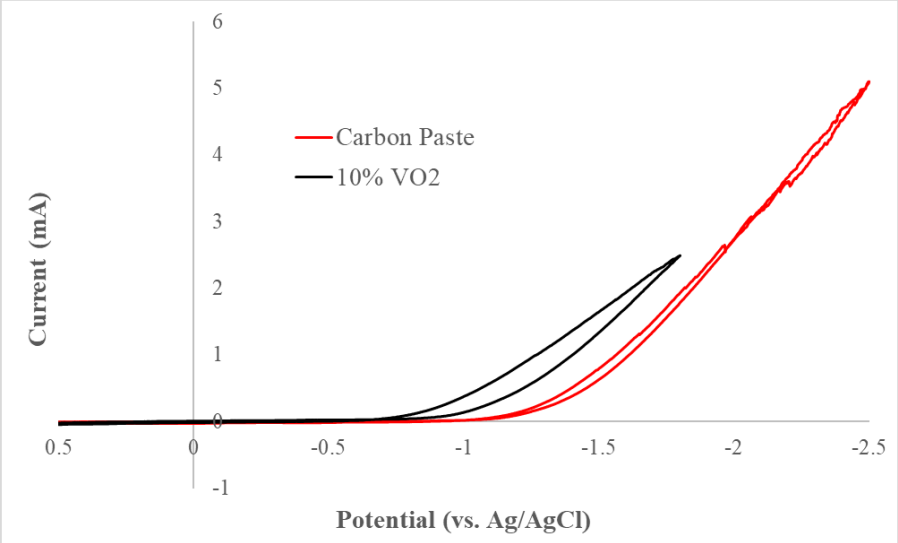


**Figure A1.2** Cyclic voltammograms comparing a carbon paste electrode and $VO_2$-modified paste electrode.

at approximately -1.0 V. Conversely, a paste electrode fabricated using 10% by mass $VO_2$ powder, showed an onset nearly 200 mV more positive at -0.8 V. The fact that the signals did not form peaks is indicative of the process not being diffusion limited. Furthermore, the lack of bubbles at the surface of the electrode suggested that the hydrogen evolution reaction (HER), which tends to be a major competing reaction that lowers the overall efficiency of $CO_2$ reduction, was not occurring.[109,120] Electrolysis was performed using both CP and $VO_2$-modified CP electrodes, however, there was insufficient time to analyze the product(s).

### *A1.4 Conclusions*

Preliminary results suggest that the inclusion of $VO_2$ into a carbon paste electrode lowers the onset of $CO_2$ reduction by approximately 200 mV, indicating that $VO_2$ may be catalytically active. Further electrolysis experiments will need to be performed to determine the product(s) of the reduction.

APPENDIX II

# SOLID-STATE RESISTIVITY OF ALKANETHIOLATE-PROTECTED GOLD NANOPARTICLES

## *A2.1 Background*

As the need for more efficient processors and electronic equipment grows, the size of the components must become ever smaller. Soon, the point will be reached where circuits will need to be designed on a molecular level. Due to their core-shell structure, monolayer-protected gold nanoparticles (MPNs) can act as nanocapacitors within a molecular circuit.[121] The gold core and external solution (if the particles are in solution) are sources of charge; if the protecting monolayer is nonconducting, those charges are separated, which is the very definition of a capacitor. A diagram showing the inclusion of MPNs in a model molecular circuit is shown in **Figure A2.1**.

Recent work in the Cliffel lab has studied the rate of electron transfer of MPNs capped with a variety of alkanethiolate ligands and highly conjugated wire-like molecules.[122] This work relied on scanning electrochemical microscopy (SECM) in order to determine the electron transfer rates. By monitoring current as a function of distance between the working and substrate electrodes, a positive or negative feedback curve is generated; electron transfer can then be numerically determined from these curves. Electron transfer rate may be considered analogous to resistivity. To this end, we cast films of MPNs and used van der Pauw four-point resistivity to determine if results in the solid state were similar to those observed in solution using SECM.

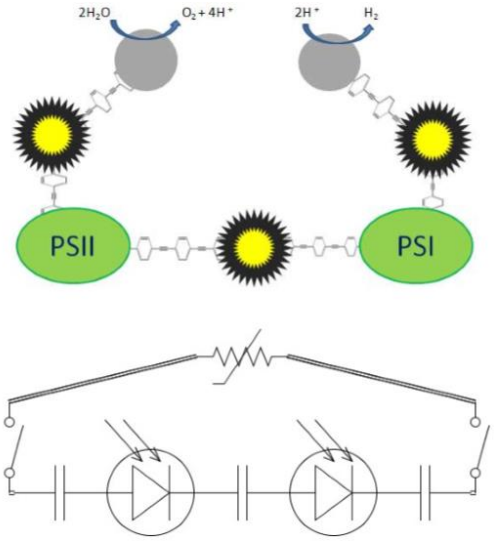


**Figure A2.1** Diagram (top) of a proposed molecular circuit integrating various nanotechnologies compared to a simplified circuit diagram (bottom). Grey circles represent Pt nanoparticles and PSI/PSII refer to photosystem proteins.[122]

### *A2.2 Methods & Materials*

Alkanethiolate MPNs were synthesized using a modified version of the two phase Brust method.[123] Briefly, 0.1 g of $HAuCl_4 \cdot 3H_2O$ was dissolved in DI water and transferred into 30 mL of toluene using the phase transfer agent, tetraoctylammonium bromide (TOAB). The organic layer was separated and cooled to 0°C and reacted with an alkanethiol (3:1, mol/mol) until colorless, signifying the reduction of $Au^{3+}$ to $Au^{+}$. After 1 min, 10 eq. chilled $NaBH_4$ dissolved in minimal water was quickly added to the reaction to completely reduce the gold and form the MPNs. After three hours, the toluene was removed via rotary evaporation, followed by addition of ethanol to remove unreacted material overnight. MPNs were then washed with acetonitrile and centrifuged. Washing was repeated 5-10 times prior to drying via rotary evaporation. Alkanethiols of varying length were used in the synthesis including butanethiol ($C_4$), hexanethiol ($C_6$), octanethiol ($C_8$), and dodecanethiol ($C_{12}$). Particles were characterized using $^1$H-NMR and TEM.

A molecular wire, S-[4-(2-phenylethynyl)phenyl]ethynylphenyl]thiol or PEPEPSH (**Figure A2.2**), was place exchanged onto the synthesized Au MPNs. 50 mg of commercially available S-[4-(2-phenylethynyl)phenyl]ethynylphenyl]thioacetate (PEPEPAsc) was added into ~10 mL of ethanol in a three-neck round bottom flask. 175 mg of NaOH dissolved in $H_2O$ was then added. This mixture was refluxed under nitrogen for two hours, after which HCl was used to neutralize the solution after cooling to room temperature. The solution was then transferred to a separatory funnel and the organic component was separated after the addition of degassed diethyl ether. The organic solution was dried over anhydrous $Na_2SO_4$, and the solvent was removed using rotary evaporation.

To perform the place exchange, 2 mg of PEPEPSH was dissolved in 5 mL of toluene and mixed with 5 mg of the MPNs in another 5 mL of toluene and stirred for 48-72 hours. Afterwards, the toluene was removed using rotary evaporation, and the nanoparticles were cleaned via centrifugation using the same solvents as mentioned previously. The ratios of wire-to-ligand were determined through $^1$H-NMR.

To make the films, the nanoparticles were dissolved to saturation in toluene (~20 mg MPN/0.1 mL).[124] 15 µL of the solution was drop cast onto microscope cover slips and immediately placed into a vacuum chamber for ~20 minutes. A Veeco Dektak 150 Stylus Profilometer was used to measure the average thickness and smoothness of each film. A scan length of 1.00 cm with a duration of 60 seconds was used at a stylus force of 3.00 mg in tapping mode. These parameters did not disrupt the contour of the film, allowing for future four-point probe analysis.

Resistivity measurements were made using a four-point method and was made under the assumption that each film was 2 µm thick (measurements were later corrected

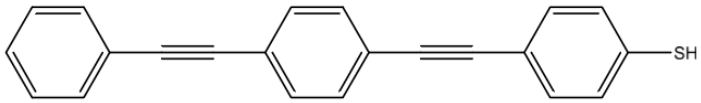


**Figure A2.2** S-[4-(2-phenylethynyl)phenyl]ethynylphenyl]thiol.

using data from profilometry). After the initial measurements (a total of eight) were made, the film was rotated 45 degrees and another measurement was taken. As such, a total of sixteen measurements per film were taken.

### *A2.3 Results*

Previous results from SECM experiments showed a decreasing electron transfer rate with increasing alkanethiolate length, which is expected based on an electron tunneling mechanism. As stated previously, electron transfer may be considered analogous to resistivity and results obtained using four-point resistivity reveal a similar trend (**Figure A2.3**). With increasing alkanethiolate length, the resistivity of the corresponding films increases significantly (slower electron transfer).

Particle films were also modified with the PEPEPSH wire molecule. $^{1}$H-NMR is capable of estimating the total ligand exchange by comparing the signal of the wire molecule, which has signal mostly in the aromatic region, to the signal in the alkane region. PEPEPSH is a rigid, fully conjugated molecule that is significantly more conductive than alkanethiolates of similar length.[125] However, because of its rigidity, it can interfere with the electron tunneling mechanism of shorter capping ligands. A comparison of $C_6$ and $C_8$ particles modified by PEPEPSH is shown in **Figure A2.4**.

As expected, when exchanged for the similarly sized $C_8$ ligands, the resistivity decreases as a result of tunneling through the conjugated rings of PEPEPS. On the other hand, when exchanged with the much shorter $C_6$ ligands, the resistivity almost doubles.

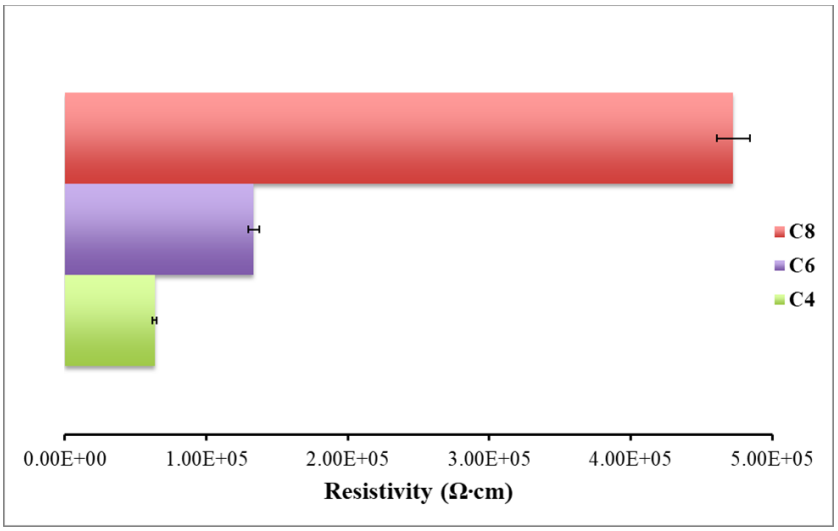


**Figure A2.3** Comparison of the resistivity of $C_4$, $C_6$, and $C_8$ monolayer protected Au nanoparticle films. Error bars represent standard error.

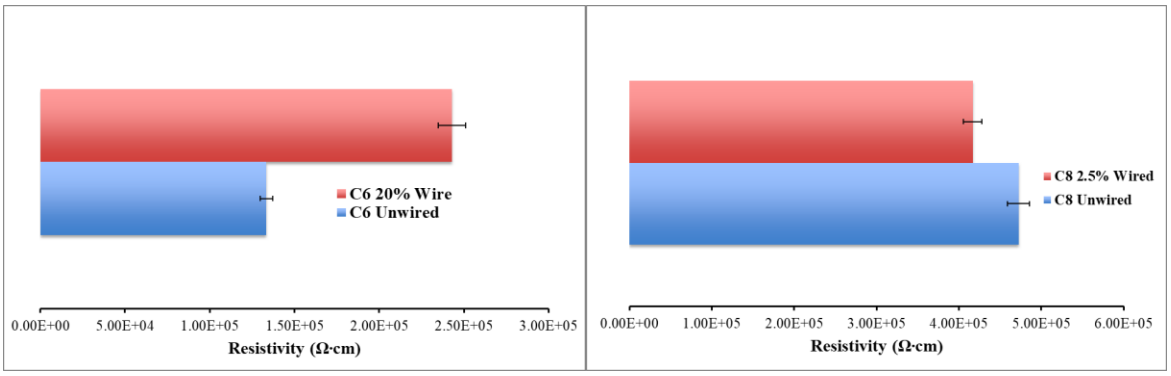


**Figure A2.4** Comparison of the resistivities of wired and unwired $C_6$-capped AuMPNs (left) and wired and unwired $C_8$-capped AuMPNs (right). Error bars represent standard error.

This may be attributed to the fact that resonant tunneling, while faster than tunneling through alkane chains, is still length dependent.[126] The rigidity may also play a factor in this increase. Crisostomo theorized that because the PEPEPS wire is almost three times longer than $C_6$, it blocked the particle from making contact with the electrode surface.[122] Similarly, in this scenario, the rigid wire may decrease packing efficiency and cause difficulty in the transfer of electrons from one particle to another due to poor contact. Several attempts were made to expand the trend out to $C_{12}$-capped nanoparticles, however reliable resistivity measurements could not be obtained, possibly because the resistivity of the films was too high.

### *A2.5 Conclusions*

Films of alkanethiolate-protected Au MPNs tested using a four-point probe showed similar trends in electron transfer as compared to previous results obtained using SECM. One disadvantage to the four-point probe is that it appears to be limited to monolayer thicknesses ranging from $C_4$ to $C_8$. Additionally, converting from resistivity to electron transfer, while simple when considering a conductive metal wire, would be incredibly difficult when taking into consideration that the films are made of billions of individual nanocapacitors. Additional considerations would need to be made in order to determine if the electron transfer rates observed in solution remain the same in a solid state film.

### *A2.6 Acknowledgements*

I would like to thank Choongwon Jin who assisted in the synthesis of the nanoparticles and PEPEPSH, as well as the film preparation.

REFERENCES


(1) Pergament, A. L.; Stefanovich, G. B.; Kuldin, N. A.; Velichko, A. A. On the Problem of Metal-Insulator Transitions in Vanadium Oxides. *ISRN Condens. Matter Phys.* **2013**, *2013*, 1–6.

(2) Schwingenschlögl, U.; Eyert, V. The Vanadium Magnéli Phases $V_nO_{2n-1}$. *Ann. der Phys.* **2004**, *13* (9), 475–510.

(3) Morin, F. J. Oxides Which Show a Metal-to-Insulator Transition at the Neel Temperature. *Phys. Rev. Lett.* **1959**, *3* (1), 34–36.

(4) Nag, J.; Haglund Jr., R. F. Synthesis of Vanadium Dioxide Thin Films and Nanoparticles. *J. Phys. Condens. Matter* **2008**, *20* (26), 264016.

(5) Lopez, R.; Haynes, T. E.; Boatner, L. A.; Feldman, L. C.; Haglund Jr., R. F. Size Effects in the Structural Phase Transition of $VO_2$ Nanoparticles. *Phys. Rev. B* **2002**, *65* (22), 224113.

(6) Carpenter, M. A.; Mathur, S.; Kolmakov, A. *Metal Oxide Nanomaterials for Chemical Sensors*, 1st ed.; Carpenter, M. A., Mathur, S., Kolmakov, A., Eds.; Springer US: New York, 2013.

(7) Ma, Z.; Zhou, B.; Ren, Y. Crystalline Mesoporous Transition Metal Oxides: Hard-Templating Synthesis and Application in Environmental Catalysis. *Front. Environ. Sci. Eng.* **2013**, *7* (3), 341–355.

(8) Chen, S.; Manders, J. R.; Tsang, S.-W.; So, F. Metal Oxides for Interface Engineering in Polymer Solar Cells. *J. Mater. Chem.* **2012**, *22*, 24202–24212.

(9) Sawa, A. Resistive Switching in Transition Metal Oxides. *Mater. Today* **2008**, *11* (6), 28–36.

(10) Lokhande, C. D.; Dubal, D. P.; Joo, O.-S. Metal Oxide Thin Film Based Supercapacitors. *Curr. Appl. Phys.* **2011**, *11* (3), 255–270.

(11) Yao, J.; Li, Y.; Massé, R. C.; Uchaker, E.; Cao, G. Revitalized Interest in Vanadium Pentoxide as Cathode Material for Lithium-Ion Batteries and Beyond. *Energy Storage Mater.* **2018**, *11*, 205–259.

(12) Warnick, K. H.; Wang, B.; Cliffel, D. E.; Wright, D. W.; Haglund, R. F.; Pantelides, S. T. Room-Temperature Reactions for Self-Cleaning Molecular Nanosensors. *Nano Lett.* **2013**, *13* (2), 798–802.

(13) Casey, M. C.; Cliffel, D. E. Surface Adsorption and Electrochemical Reduction of 2,4,6- Trinitrotoluene on Vanadium Dioxide. *Anal. Chem.* **2015**, *87*, 334–337.

(14) Wu, C.; Feng, F.; Xie, Y. Design of Vanadium Oxide Structures with Controllable Electrical Properties for Energy Applications. *Chem. Soc. Rev.* **2013**, *42* (12), 5157–5183.

(15) Goodenough, J. B. Anomalous Properties of the Vanadium Oxides. *Annu. Rev. Mater. Sci.* **1971**, *1* (1), 101–138.

(16) Wu, C.; Zhang, X.; Dai, J.; Yang, J.; Wu, Z.; Wei, S.; Xie, Y. Direct Hydrothermal Synthesis of Monoclinic $VO_2$(M) Single-Domain Nanorods on Large Scale Displaying Magnetocaloric Effect. *J. Mater. Chem.* **2011**, *21* (12), 4509–4517.

(17) Goodenough, J. B. The Two Components of the Crystallographic Transition in $VO_2$. *J. Solid State Chem.* **1971**, *3* (4), 490–500.

(18) Booth, J. M.; Casey, P. S. Anisotropic Structure Deformation in the $VO_2$ Metal-Insulator Transition. *Phys. Rev. Lett.* **2009**, *103*, 086402.

(19) Hoffmann, R. How Chemistry and Physics Meet in the Solid State. *Angew. Chemie Int. Ed. English* **1987**, *26* (9), 846–878.

(20) Wentzcovitch, R. M.; Schulz, W. W.; Allen, P. B. $VO_2$: Peierls or Mott-Hubbard? A View from Band Theory. *Phys. Rev. Lett.* **1994**, *72* (21), 3389–3392.

(21) Whittaker, L.; Jaye, C.; Fu, Z.; Fischer, D. A.; Banerjee, S. Depressed Phase Transition in Solution-Grown $VO_2$ Nanostructures. *J. Am. Chem. Soc.* **2009**, *131* (18), 8884–8894.

(22) Guo, H.; Chen, K.; Oh, Y.; Wang, K.; Dejoie, C.; Syed Asif, S. A.; Warren, O. L.; Shan, Z. W.; Wu, J.; Minor, A. M. Mechanics and Dynamics of the Strain-Induced M1-M2 Structural Phase Transition in Individual $VO_2$ Nanowires. *Nano Lett.* **2011**, *11* (8), 3207–3213.

(23) Qazilbash, M. M.; Brehm, M.; Chae, B.-G.; Ho, P.-C.; Andreev, G. O.; Kim, B.-J.; Yun, S. J.; Balatsky, A. V.; Maple, M. B.; Keilmann, F.; Kim, H.-T.; Basov, D. N. Mott Transition in $VO_2$ Revealed by Infrared Spectroscopy and Nano-Imaging. *Science (80-. ).* **2007**, *318*, 1750–1753.

(24) Hubbard, J. Electron Correlations in Narrow Energy Bands. In *Proceedings of the Royal Society of London. Series A, Mathematical and Physical Sciences*; 1963; Vol. 276, pp 238–257.

(25) Kim, S.; Kim, K.; Kang, C.-J.; Min, B. I. Correlation-Assisted Phonon Softening and the Orbital-Selective Peierls Transition in $VO_2$. *Phys. Rev. B* **2013**, *87* (19), 195106.

(26) Driscoll, T.; Kim, H.-T.; Chae, B.-G.; Kim, B.-J.; Lee, Y.-W.; Jokerst, N. M.; Palit, S.; Smith, D. R.; Di Ventra, M.; Basov, D. N. Memory Metamaterials. *Science* **2009**, *325*, 1518–1522.

(27) Coy, H.; Cabrera, R.; Sepúlveda, N.; Fernández, F. E. Optoelectronic and All-Optical Multiple Memory States in Vanadium Dioxide. *J. Appl. Phys.* **2010**, *108*, 113115.

(28) Yang, Z.; Ko, C.; Ramanathan, S. Oxide Electronics Utilizing Ultrafast Metal-Insulator Transitions. *Annu. Rev. Mater. Res.* **2011**, *41*, 337–367.

(29) Gao, Y.; Luo, H.; Zhang, Z.; Kang, L.; Chen, Z.; Du, J.; Kanehira, M.; Cao, C. Nanoceramic $VO_2$ Thermochromic Smart Glass: A Review on Progress in Solution Processing. *Nano Energy* **2012**, *1* (2), 221–246.

(30) Li, S.-Y.; Niklasson, G. A.; Granqvist, C. G. Thermochromic Fenestration with $VO_2$-Based Materials: Three Challenges and How They Can Be Met. *Thin Solid Films* **2012**, *520* (10), 3823–3828.

(31) Zhang, Y.; Zhang, J.; Zhang, X.; Huang, C.; Zhong, Y.; Deng, Y. The Additives W, Mo, Sn and Fe for Promoting the Formation of $VO_2$(M) and Its Optical Switching Properties. *Mater. Lett.* **2013**, *92*, 61–64.

(32) Oka, Y.; Sato, S.; Yao, T.; Yamamoto, N. Crystal Structures and Transition Mechanism of $VO_2$(A). *J. Solid State Chem.* **1998**, *141* (2), 594–598.

(33) Théobald, F.; Cabala, R.; Bernard, J. Essai Sur La Structure de $VO_2$(B). *J. Solid State Chem.* **1976**, *17* (4), 431–438.

(34) Andersson, G. Studies on Vanadium Oxides II. The Crystal Structure of Vanadium Dioxide. *Acta Chem. Scand.* **1956**, *10* (4), 623–628.

(35) Chamberland, B. L. New Defect Vanadium Dioxide Phases. *J. Solid State Chem.* **1973**, *7* (4), 377–384.

(36) McWhan, D. B.; Marezio, M.; Remeika, J. P.; Dernier, P. D. X-Ray Diffraction Study of Metallic $VO_2$. *Phys. Rev. B* **1974**, *10* (2), 490–495.

(37) Hagrman, D.; Zubieta, J.; Warren, C. J.; Meyer, L. M.; Treacy, M. M. J.; Haushalter, R. C. A New Polymorph of $VO_2$ Prepared by Soft Chemical Methods. *J. Solid State Chem.* **1998**, *138*, 178–182.

(38) Liu, L.; Cao, F.; Yao, T.; Xu, Y.; Zhou, M.; Qu, B.; Pan, B.; Wu, C.; Wei, S.; Xie, Y. New-Phase $VO_2$ Micro/Nanostructures: Investigation of Phase Transformation and Magnetic Property. *New J. Chem.* **2012**, *36* (3), 619–625.

(39) Santulli, A. C.; Xu, W.; Parise, J. B.; Wu, L.; Aronson, M. C.; Zhang, F.; Nam, C.-Y.; Black, C. T.; Tiano, A. L.; Wong, S. S. Synthesis and Characterization of $V_2O_3$ Nanorods. *Phys. Chem. Chem. Phys.* **2009**, *11* (19), 3718–3726.

(40) Dai, L.; Gao, Y.; Cao, C.; Chen, Z.; Luo, H.; Kanehira, M.; Jin, J.; Liu, Y. $VO_2$(A) Nanostructures with Controllable Feature Sizes and Giant Aspect Ratios: One-Step Hydrothermal Synthesis and Lithium-Ion Battery Performance. *RSC Adv.* **2012**, *2* (12), 5265–5270.

(41) Son, J.-H.; Wei, J.; Cobden, D.; Cao, G.; Xia, Y. Hydrothermal Synthesis of Monoclinic $VO_2$ Micro- and Nanocrystals in One Step and Their Use in Fabricating Inverse Opals. *Chem. Mater.* **2010**, *22* (10), 3043–3050.

(42) Popuri, S. R.; Miclau, M.; Artemenko, A.; Labrugere, C.; Villesuzanne, A.; Pollet, M. Rapid Hydrothermal Synthesis of $VO_2$(B) and Its Conversion to Thermochromic $VO_2(M_1)$. *Inorg. Chem.* **2013**, *52* (9), 4780–4785.

(43) Zhang, Y.; Zhang, J.; Zhang, X.; Mo, S.; Wu, W.; Niu, F.; Zhong, Y.; Liu, X.; Huang, C.; Liu, X. Direct Preparation and Formation Mechanism of Belt-like Doped $VO_2$(M) with Rectangular Cross Sections by One-Step Hydrothermal Route and Their Phase Transition and Optical Switching Properties. *J. Alloys Compd.* **2013**, *570*, 104–113.

(44) Zhou, X.; Wei, C.; Li, M.; Qiu, S.; Li, X. Thermodynamics of Vanadium-Sulfur-Water Systems at 298 K. *Hydrometallurgy* **2011**, *106* (1–2), 104–112.

(45) Suh, J. Y.; Lopez, R.; Feldman, L. C.; Haglund, R. F. Semiconductor to Metal Phase Transition in the Nucleation and Growth of $VO_2$ Nanoparticles and Thin Films. *J. Appl. Phys.* **2004**, *96* (2), 1209–1213.

(46) Ji, S.; Zhao, Y.; Zhang, F.; Jin, P. Direct Formation of Single Crystal $VO_2$(R) Nanorods by One-Step Hydrothermal Treatment. *J. Cryst. Growth* **2010**, *312* (2), 282–286.

(47) Tan, X.; Yao, T.; Long, R.; Sun, Z.; Feng, Y.; Cheng, H.; Yuan, X.; Zhang, W.; Liu, Q.; Wu, C.; Xie, Y.; Wei, S. Unraveling Metal-Insulator Transition Mechanism of $VO_2$ Triggered by Tungsten Doping. *Sci. Rep.* **2012**, *2*, 466.

(48) van der Pauw, L. J. A Method of Measuring Specific Resistivity and Hall Effect of Discs of Arbitrary Shape. *Philips Res. Reports* **1958**, *13* (1), 1–9.

(49) van der Pauw, L. J. A Method of Measuring the Resistivity and Hall Coefficient on Lamellae of Arbitrary Shape. *Philips Tech. Rev.* **1958**, *20* (I), 220–224.

(50) Carminati, R.; Nieto-Vesperinas, M.; Greffet, J.-J. Reciprocity of Evanescent Electromagnetic Waves. *J. Opt. Soc. Am. A* **1998**, *15* (3), 706–712.

(51) Seebeck, T. J. Magnetische Polarisation Der Metalle Und Erze Durch Temperatur-Differenz. In *Abhandlungen der Königlichen Akademie der Wissenschaften zu Berlin*; Berlin, 1822; pp 265–373.

(52) Watson, E. S.; O'Neill, M. J. Differential Microcalorimeter. 3,263,484, 1962.

(53) Brennan, W. P. Some Applications of Differential Scanning Calorimetry for the Analysis of Polymers. *Thermochim. Acta* **1976**, *17*, 285–293.

(54) Suh, J. Y.; Donev, E. U.; Lopez, R.; Feldman, L. C.; Haglund Jr., R. F. Modulated Optical Transmission of Subwavelength Hole Arrays in Metal-$VO_2$ Films. *Appl. Phys. Lett.* **2006**, *88* (13), 133115.

(55) Liu, M.; Hwang, H. Y.; Tao, H.; Strikwerda, A. C.; Fan, K.; Keiser, G. R.; Sternbach, A. J.; West, K. G.; Kittiwatanakul, S.; Lu, J.; Wolf, S. A.; Omenetto, F. G.; Zhang, X.; Nelson, K. A.; Averitt, R. D. Terahertz-Field-Induced Insulator-to-Metal Transition in Vanadium Dioxide Metamaterial. *Nature* **2012**, *487* (7407), 345–348.

(56) Driscoll, T.; Palit, S.; Qazilbash, M. M.; Brehm, M.; Keilmann, F.; Chae, B.-G.; Yun, S.-J.; Kim, H.-T.; Cho, S. Y.; Jokerst, N. M.; Smith, D. R.; Basov, D. N. Dynamic Tuning of an Infrared Hybrid-Metamaterial Resonance Using Vanadium Dioxide. *Appl. Phys. Lett.* **2008**, *93* (2), 024101.

(57) Kruger, B. A.; Joushaghani, A.; Poon, J. K. S. Design of Electrically Driven Hybrid Vanadium Dioxide ($VO_2$) Plasmonic Switches. *Opt. Express* **2012**, *20* (21), 23598–23609.

(58) Soukoulis, C. M.; Wegener, M. Past Achievements and Future Challenges in the Development of Three-Dimensional Photonic Metamaterials. *Nat. Photonics* **2011**, *5*, 523–530.

(59) Zheludev, N. I.; Kivshar, Y. S. From Metamaterials to Metadevices. *Nat. Mater.* **2012**, *11* (11), 917–924.

(60) Kats, M. A.; Sharma, D.; Lin, J.; Genevet, P.; Blanchard, R.; Yang, Z.; Qazilbash, M. M.; Basov, D. N.; Ramanathan, S.; Capasso, F. Ultra-Thin Perfect Absorber Employing a Tunable Phase Change Material. *Appl. Phys. Lett.* **2012**, *101* (22), 221101.

(61) Dicken, M. J.; Aydin, K.; Pryce, I. M.; Sweatlock, L. A.; Boyd, E. M.; Walavalkar, S.; Ma, J.; Atwater, H. A. Frequency Tunable Near-Infrared Metamaterials Based on $VO_2$ Phase Transition. *Opt. Express* **2009**, *17* (20), 18330–18339.

(62) Ferrara, D. W.; Nag, J.; MacQuarrie, E. R.; Kaye, A. B.; Haglund, Jr., R. F. Plasmonic Probe of the Semiconductor to Metal Phase Transition in Vanadium Dioxide. *Nano Lett.* **2013**, *13* (9), 4169–4175.

(63) Leroux, C.; Nihoul, G.; Van Tendeloo, G. From $VO_2$(B) to $VO_2$(R): Theoretical Structures of $VO_2$ Polymorphs and in Situ Electron Microscopy. *Phys. Rev. B* **1998**, *57* (9), 5111–5121.

(64) Xiao, X.; Cheng, H.; Dong, G.; Yu, Y.; Chen, L.; Miao, L.; Xu, G. A Facile Process to Prepare One Dimension $VO_2$ Nanostructures with Superior Metal–semiconductor Transition. *CrystEngComm* **2013**, *15* (6), 1095–1106.

(65) Gui, Z.; Fan, R.; Mo, W.; Chen, X.; Yang, L.; Zhang, S.; Hu, Y.; Wang, Z.; Fan, W. Precursor Morphology Controlled Formation of Rutile $VO_2$ Nanorods and Their Self-Assembled Structure. *Chem. Mater.* **2002**, *14*, 5053–5056.

(66) Zhu, C.; Kaur, M.; Tang, F.; Liu, X.; Smith, D. J.; Nemanich, R. J. Band Alignment of Vanadium Oxide as an Interlayer in a Hafnium Oxide-Silicon Gate Stack Structure. *J. Appl. Phys.* **2012**, *112* (8), 084105.

(67) LaMer, V. K. Nucleation in Phase Transitions. *Ind. Eng. Chem.* **1952**, *44* (6), 1270–1277.

(68) Ji, S.; Zhang, F.; Jin, P. Selective Formation of $VO_2$(A) or $VO_2$(R) Polymorph by Controlling the Hydrothermal Pressure. *J. Solid State Chem.* **2011**, *184* (8), 2285–2292.

(69) LaMer, V. K.; Dinegar, R. H. Theory, Production, and Mechanism of Formation of Monodispersed Hydrosols. *J. Am. Chem. Soc.* **1950**, *72* (11), 4847–4854.

(70) Cao, C.; Gao, Y.; Luo, H. Pure Single-Crystal Rutile Vanadium Dioxide Powders: Synthesis, Mechanism and Phase-Transformation Property. *J. Phys. Chem. C* **2008**, *112* (48), 18810–18814.

(71) Pashkin, A.; Kübler, C.; Ehrke, H.; Lopez, R.; Halabica, A.; Haglund Jr., R. F.; Huber, R.; Leitenstorfer, A. Ultrafast Insulator-Metal Phase Transition in $VO_2$ Studied by Multiterahertz Spectroscopy. *Phys. Rev. B* **2011**, *83*, 1–10.

(72) Narayan, J.; Bhosle, V. M. Phase Transition and Critical Issues in Structure-Property Correlations of Vanadium Oxide. *J. Appl. Phys.* **2006**, *100* (10), 103524.

(73) Paik, T.; Hong, S.-H.; Gaulding, E. A.; Caglayan, H.; Gordon, T. R.; Engheta, N.; Kagan, C. R.; Murray, C. B. Solution-Processed Phase-Change $VO_2$ Metamaterials from Colloidal Vanadium Oxide ($VO_x$) Nanocrystals. *ACS Nano* **2014**, *8* (1), 797–806.

(74) Whittaker, L.; Velazquez, J. M.; Banerjee, S. A VO-Seeded Approach for the Growth of Star-Shaped $VO_2$ and $V_2O_5$ Nanocrystals: Facile Synthesis, Structural Characterization, and Elucidation of Electronic Structure. *CrystEngComm* **2011**, *13* (17), 5328.

(75) Zou, J.; Peng, Y.; Lin, H. A Low-Temperature Synthesis of Monoclinic $VO_2$ in an Atmosphere of Air. *J. Mater. Chem. A* **2013**, *1* (13), 4250–4254.

(76) Horrocks, G. A.; Singh, S.; Likely, M. F.; Sambandamurthy, G.; Banerjee, S. Scalable Hydrothermal Synthesis of Free-Standing $VO_2$ Nanowires in the M1 Phase. *ACS Appl. Mater. Interfaces* **2014**, *6*, 15726–15732.

(77) Brassard, D.; Fourmaux, S.; Jean-Jacques, M.; Kieffer, J. C.; El Khakani, M. A. Grain Size Effect on the Semiconductor-Metal Phase Transition Characteristics of Magnetron-Sputtered $VO_2$ Thin Films. *Appl. Phys. Lett.* **2005**, *87* (5), 051910.

(78) Scherrer, P. Bestimmung Der Grösse Und Der Inneren Struktur von Kolloidteilchen Mittels Röntgenstrahlen. *Nachr. Ges. Wiss. Göttingen* **1918**, *26*, 98–100.

(79) Langford, J. I.; Wilson, A. J. C. Scherrer after Sixty Years: A Survey and Some New Results in the Determination of Crystallite Size. *J. Appl. Crystallogr.* **1978**, *11*, 102–113.

(80) Donev, E. U.; Ziegler, J. I.; Haglund Jr., R. F.; Feldman, L. C. Size Effects in the Structural Phase Transition of $VO_2$ Nanoparticles Studied by Surface-Enhanced Raman Scattering. *J. Opt. A Pure Appl. Opt.* **2009**, *11* (12), 125002.

(81) Zhang, S.; Shang, B.; Yang, J.; Yan, W.; Wei, S.; Xie, Y. From $VO_2$(B) to $VO_2$(A) Nanobelts: First Hydrothermal Transformation, Spectroscopic Study and First Principles Calculation. *Phys. Chem. Chem. Phys.* **2011**, *13* (35), 15873–15881.

(82) Lewis, T. A.; Newcombe, D. A.; Crawford, R. L. Bioremediation of Soils Contaminated with Explosives. *J. Environ. Manage.* **2004**, *70*, 291–307.

(83) Sabbioni, G.; Liu, Y.-Y.; Yan, H.; Sepai, O. Hemoglobin Adducts, Urinary Metabolites and Health Effects in 2,4,6-Trinitrotoluene Exposed Workers. *Carcinogenesis* **2005**, *26* (7), 1272–1279.

(84) *Innovative Treatment Technologies: Annual Status Report*, 8th ed.; U.S. Environmental Protection Agency, 1996.

(85) Pennington, J. C.; Brannon, J. M. Environmental Fate of Explosives. *Thermochim. Acta* **2002**, *384*, 163–172.

(86) Yinon, J. Field Detection and Monitoring of Explosives. *Trends Anal. Chem.* **2002**, *21* (4), 292–301.

(87) Wang, J. Electrochemical Sensing of Explosives. *Electroanalysis* **2007**, *19* (4), 415–423.

(88) Chua, C. K.; Pumera, M.; Rulíšek, L. Reduction Pathways of 2,4,6-Trinitrotoluene: An Electrochemical and Theoretical Study. *J. Phys. Chem. C* **2012**, *116* (6), 4243–4251.

(89) Toh, H. S.; Ambrosi, A.; Pumera, M. Electrocatalytic Effect of ZnO Nanoparticles on Reduction of Nitroaromatic Compounds. *Catal. Sci. Technol.* **2013**, *3*, 123–127.

(90) Schmelling, D. C.; Gray, K. A.; Kamat, P. V. Role of Reduction in the Photocatalytic Degradation of TNT. *Environ. Sci. Technol.* **1996**, *30* (8), 2547–2555.

(91) Filanovsky, B.; Markovsky, B.; Bourenko, T.; Perkas, N.; Persky, R.; Gedanken, A.; Aurbach, D. Carbon Electrodes Modified with $TiO_2$/Metal Nanoparticles and Their Application for the Detection of Trinitrotoluene. *Adv. Funct. Mater.* **2007**, *17* (9), 1487–1492.

(92) Marvel, R. E.; Appavoo, K.; Choi, B. K.; Nag, J.; Haglund Jr., R. F. Electron-Beam Deposition of Vanadium Dioxide Thin Films. *Appl. Phys. A* **2013**, *111* (3), 975–981.

(93) Moulder, J. F.; Stickle, W. F.; Sobol, P. E.; Bomben, K. D. *Handbook of X-Ray Photoelectron Spectroscopy*; Chastain, J., Ed.; Physical Electronics USA, Inc.: Chanhassen, Minnesota, 1995.

(94) Bard, A.; Faulkner, L. *Electrochemical Methods: Fundamentals and Applications*, 2nd ed.; Harris, D., Swain, E., Aiello, E., Eds.; John Wiley & Sons: New York, 1980.

(95) Wang, J. *Analytical Electrochemistry*, 2nd ed.; Wiley-VCH: New York, 2000.

(96) Haruta, M. Catalysis of Gold Nanoparticles Deposited on Metal Oxides. *CATTECH* **2002**, *6* (3), 102–115.

(97) Budzianowski, W. M. Value-Added Carbon Management Technologies for Low $CO_2$ Intensive Carbon-Based Energy Vectors. *Energy* **2012**, *41* (1), 280–297.

(98) Wu, H.; Zhang, N.; Wang, H.; Hong, S. Adsorption of $CO_2$ on $Cu_2O$ (111) Oxygen-Vacancy Surface: First-Principles Study. *Chem. Phys. Lett.* **2013**, *568–569*, 84–89.

(99) Zhang, C.; Yang, Q.; Koughia, C.; Ye, F.; Sanayei, M.; Wen, S.-J.; Kasap, S. Characterization of Vanadium Oxide Thin Films with Different Stoichiometry Using Raman Spectroscopy. *Thin Solid Films* **2016**, *620*, 64–69.

(100) Liu, M.; Xiang, Z.; Piao, J.; Shi, J.; Liang, Z. Electrochemistry of Vanadium Redox Couples on Nitrogen-Doped Carbon. *Electrochim. Acta* **2018**, *259*, 687–693.

(101) Ji, S.; Zhang, F.; Jin, P. Phase Transition of Single Crystal $VO_2$(R) Nanorods in Solution Revealed by Reversible Change in Surface Charge State and Structure. *Mater. Lett.* **2011**, *65* (4), 708–711.

(102) Gao, Y.; Cao, C.; Dai, L.; Luo, H.; Kanehira, M.; Ding, Y.; Wang, Z. L. Phase and Shape Controlled $VO_2$ Nanostructures by Antimony Doping. *Energy Environ. Sci.* **2012**, *5* (9), 8708–8715.

(103) Deegan, R. D.; Bakajin, O.; Dupont, T. F.; Huber, G.; Nagel, S. R.; Witten, T. A. Capillary Flow as the Cause of Ring Stains from Dried Liquid Drops. *Nature* **1997**, *389*, 827–829.

(104) McGahan, C.; Gamage, S.; Liang, J.; Cross, B.; Marvel, R. E.; Haglund, R. F.; Abate, Y. Geometric Constraints on Phase Coexistence in Vanadium Dioxide Single Crystals. *Nanotechnology* **2017**, *28*, 085701.

(105) Zhang, S.; Kang, P.; Ubnoske, S.; Brennaman, M. K.; Song, N.; House, R. L.; Glass, J. T.; Meyer, T. J. Polyethylenimine-Enhanced Electrocatalytic Reduction of $CO_2$ to Formate at Nitrogen-Doped Carbon Nanomaterials. *J. Am. Chem. Soc.* **2014**, *136* (22), 7845–7848.

(106) Oloman, C.; Li, H. Electrochemical Processing of Carbon Dioxide. *ChemSusChem* **2008**, *1* (5), 385–391.

(107) Hori, Y.; Wakebe, H.; Tsukamoto, T.; Koga, O. Electrocatalytic Process of CO Selectivity in Electrochemical Reduction of $CO_2$ at Metal Electrodes in Aqueous Media. *Electrochim. Acta* **1994**, *39* (11/12), 1833–1839.

(108) Lim, R. J.; Xie, M.; Sk, M. A.; Lee, J.-M.; Fisher, A.; Wang, X.; Lim, K. H. A Review on the Electrochemical Reduction of $CO_2$ in Fuel Cells, Metal Electrodes and Molecular Catalysts. *Catal. Today* **2014**, *233*, 169–180.

(109) Lu, Q.; Rosen, J.; Jiao, F. Nanostructured Metallic Electrocatalysts for Carbon Dioxide Reduction. *ChemCatChem* **2015**, *7* (1), 38–47.

(110) Khezri, B.; Fisher, A. C.; Pumera, M. $CO_2$ Reduction: The Quest for Electrocatalytic Materials. *J. Mater. Chem. A* **2017**, *5*, 8230–8246.

(111) Lee, S.; Fan, C.; Wu, T.; Anderson, S. L. CO Oxidation on $Au_n/TiO_2$ Catalysts Produced by Size-Selected Cluster Deposition. *J. Am. Chem. Soc.* **2004**, *126* (18), 5682–5683.

(112) Ke, J.; Xiao, J.-W.; Zhu, W.; Liu, H.; Si, R.; Zhang, Y.-W.; Yan, C.-H. Dopant-Induced Modification of Active Site Structure and Surface Bonding Mode for High-Performance Nanocatalysts: CO Oxidation on Capping-Free (110)-Oriented $CeO_2$:Ln (Ln = La−Lu) Nanowires. *J. Am. Chem. Soc.* **2013**, *135*, 15191–15200.

(113) Casey, M. C. Investigations of Vanadium Dioxide as a Catalytic Electrode and Support, Vanderbilt, 2015.

(114) Simard, S.; Gallant, D. A Study of the Electrochemical Behavior of Cobalt in Aqueous $H_2CO_3/HCO_3^-/CO_3^{2-}$ Solutions at PH 7-9. *Can. J. Chem.* **2004**, *82* (5), 583–594.

(115) Bachmeier, A.; Hall, S.; Ragsdale, S. W.; Armstrong, F. A. Selective Visible Light-Driven $CO_2$ Reduction on a p-Type Dye-Sensitized NiO Photocathode. *J. Am. Chem. Soc.* **2014**, *136*, 13518–13521.

(116) Li, C. W.; Kanan, M. W. $CO_2$ Reduction at Low Overpotential on Cu Electrodes Resulting from the Reduction of Thick $Cu_2O$ Films. *J. Am. Chem. Soc.* **2012**, *134*, 7231–7234.

(117) Popić, J. P.; Avramov-Ivić, M. L.; Vuković, N. B. Reduction of Carbon Dioxide on Ruthenium Oxide and Modified Ruthenium Oxide Electrodes in 0.5 M $NaHCO_3$. *J. Electroanal. Chem.* **1997**, *421*, 105–110.

(118) Andersen, C. B. Understanding Carbonate Equilibria by Measuring Alkalinity in Experimental and Natural Systems. *J. Geosci. Educ.* **2002**, *50* (4), 389–403.

(119) Sander, R. Compilation of Henry's Law Constants (Version 4.0) for Water as Solvent. *Atmostpheric Chem. Phys.* **2015**, *15* (8), 4399–4981.

(120) Sreekanth, N.; Phani, K. L. Selective Reduction of $CO_2$ to Formate through Bicarbonate Reduction on Metal Electrodes: New Insights Gained from SG/TC Mode of SECM. *Chem. Commun.* **2014**, *50* (76), 11143–11146.

(121) Chen, S.; Murray, R. W.; Feldberg, S. W. Quantized Capacitance Charging of Monolayer-Protected Au Clusters. *J. Phys. Chem. B* **1998**, *102*, 9898–9907.

(122) Crisostomo, D. A. Scanning Electrochemical Microscopy Investigations of Monolayer-Protected Gold Nanoparticles and Shewanella Oneidensis, Vanderbilt, 2016.

(123) Brust, M.; Walker, M.; Bethell, D.; Schiffrin, D. J.; Whyman, R. Synthesis of Thiol-Derivatised Gold Nanoparticles in a Two-Phase Liquid-Liquid System. *J. Chem. Soc. Chem. Commun.* **1994**, 801–802.

(124) Wuelfing, W. P.; Murray, R. W. Electron Hopping through Films of Arenethiolate Monolayer-Protected Gold Clusters. *J. Phys. Chem. B* **2002**, *106*, 3139–3145.

(125) Kushmerick, J. G.; Pollack, S. K.; Yang, J. C.; Naciri, J.; Holt, D. B.; Ratner, M. A.; Shashidhar, R. Understanding Charge Transport in Molecular Electronics. *Ann. N. Y. Acad. Sci.* **2003**, *1006*, 277–290.

(126) Berlin, Y. A.; Hutchison, G. R.; Rempala, P.; Ratner, M. A.; Michl, J. Charge Hopping in Molecular Wires as a Sequence of Electron-Transfer Reactions. *J. Phys. Chem. A* **2003**, *107*, 3970–3980.

# Aaron W. Daniel

Vanderbilt University, Department of Chemistry, 7330 Stevenson Center, Nashville, TN 37235

E-mail
aaron.w.daniel@gmail.com


## Education

VANDERBILT UNIVERSITY, Nashville, TN ***August 2018***
***Doctor of Philosophy in Chemistry***
Dissertation Title: Hydrothermal Synthesis of Phase-Changing Vanadium Dioxide Nanoparticles and Their Use in Environmental Remediation

WESTERN KENTUCKY UNIVERSITY, Bowling Green, KY ***May 2012***
***Bachelor of Science in Chemistry with Minor in Mathematics (Honors)***

## Research Experience

VANDERBILT UNIVERSITY, Nashville, TN ***March 2013 – Present***
***Advisor: Dr. David E. Cliffel***

- Devised a hydrothermal route to reliably synthesize phase-changing vanadium dioxide nanoparticles.
- Evaluated the feasibility of using vanadium dioxide as an electrode material for electrocatalytic reactions including the detection and reduction of 2,4,6-trinitrotoluene, electroreduction of carbon dioxide, and electroreduction of oxygen.

WESTERN KENTUCKY UNIVERSITY, Bowling Green, KY ***January 2010 – May 2012***
***Advisor: Dr. Jeremy B. Maddox***

- Modeled organometallic, heterocyclic monomer species to determine their possible application as polymer candidates in organic photovoltaics.
- Developed a Morse oscillator model for calculating stationary state wave functions and reaction probabilities in a multi-dimensional reactive scattering system.

NATIONAL CHUNG HSING UNIVERSITY, Taichung, Taiwan ***2011 (May – June)***
***Advisor: Dr. Wei-Ping Dow***

- Used cyclic voltammetry with a novel electrode to determine the electrochemical reactivity of various phenolic compounds.
- Gained invaluable experience in working in an international setting.

## Selected Poster & Oral Presentations

- "Electrochemical Detection of TNT Using Vanadium Dioxide Particle Films" (oral) **Aaron W. Daniel**. Vanderbilt Institute for Nanoscale Science & Engineering Summer Seminar Series (invited) 2017.

- "Electrochemical Detection of TNT Using Vanadium Dioxide Particle Films" (oral) **Aaron W. Daniel**. Southeast Regional Meeting of the ACS (SERMACS) 2015 in Memphis, TN.

- "Electrochemical Detection of TNT Using Vanadium Dioxide Particle Films" (poster) **Aaron W. Daniel**. TNSCORE 2015 Annual Meeting in Nashville, TN.

- "Formation of Phase-Changing Vanadium Dioxide Nano-Asterisks" (poster) **Aaron W. Daniel** & David E. Cliffel. Pittsburgh Conference on Analytical Chemistry and Applied Spectroscopy (Pittcon) 2015 in New Orleans, LA.

- "Formation of Phase-Changing Vanadium Dioxide Nano-Asterisks" (poster) **Aaron W. Daniel** & David E. Cliffel. Southeast Regional Meeting of the ACS (SERMACS) 2014 in Nashville, TN.

## Publications

- **Daniel, A. W.**; Casey, M. C.; Cliffel, D. E. Formation of phase changing vanadium dioxide nano-asterisks. *In preparation for ACS Omega*.

- **Daniel, A. W.**; Cliffel, D. E. Vanadium Dioxide as an Electrocatalyst for the Detection and Reduction of 2,4,6-trinitrotoluene. *In preparation for Analytical Chemistry*.

- Snyder, C. A.; Tice, N. C.; Maddox, J. B.; Parkin, S.; **Daniel, A. W.**; Thomas, J. M. Synthesis, structure, and theoretical calculations of 1η-3,7-difurylcyclopenta[3,4-d]pyridazine. *Heterocycles* **2011**, *83*, 1275-1290.

## Teaching Experience

VANDERBILT UNIVERSITY, Nashville, TN ***August 2012 – December 2017***

***Graduate Teaching Assistant (General Chemistry Lab)***

Work included preparing a 10-15 minute lecture before lab explaining the theory of the experiment, ensuring that all students observed proper lab safety and laboratory techniques, and grading weekly lab reports.

***Graduate Teaching Fellow (Advanced Integrated Lab)***

Capstone GTF positions were reserved for seasoned graduate students who have excelled both in their own research and in previous teaching responsibilities. As a Capstone GTF, I regularly met with several undergraduate seniors and assisted them in designing and carrying out an original research project.

WESTERN KENTUCKY UNIVERSITY, Bowling Green, KY ***August 2009 – May 2012***

***Math Lab Tutor***

Work included tutoring students in math courses such as: Remedial Math, College Algebra, Trigonometry, Calculus I, and Calculus II.

## Activities

- Member of American Chemical Society (2010 – present)
- Volunteer for Vanderbilt Summer Academy (2014 – 2018)